

## Wall shear stress and wall heat flux in a supersonic turbulent boundary layer subjected to concave surface curvature

Fulin Tong (童福林),<sup>1</sup> Junyi Duan (段俊亦),<sup>2,3</sup> Xiangxin Ji (纪相鑫) ,<sup>2,3</sup> Siwei Dong (董思卫),<sup>1</sup> Xianxu Yuan (袁先旭),<sup>1,\*</sup> and Xinliang Li (李新亮)<sup>2,3</sup>

<sup>1</sup>State Key Laboratory of Aerodynamics, Mianyang 621000, China

<sup>2</sup>LHD, Institute of Mechanics, Chinese Academy of Sciences, Beijing 100190, China

<sup>3</sup>School of Engineering Science, University of Chinese Academy of Sciences, Beijing 100049, China



(Received 18 June 2023; accepted 7 November 2023; published 5 December 2023)

Direct numerical simulation is employed to investigate the characteristics of wall shear stress (WSS) and wall heat flux (WHF) beneath a spatially developing supersonic turbulent boundary layer with a cold-wall thermal condition subjected to a concavely curved compression ramp with a deflection angle of  $24^\circ$ . The Mach number is 2.25 and the friction Reynolds number is 769. Numerical data are exploited to characterize the effect of the concave surface curvature on the statistical and structural properties of the fluctuating WSS and WHF, including the probability density function, space-time correlations, and frequency spectra. Across the curved region, the occurrence probability of extreme negative events is strongly affected by the curvature, as manifested by a noticeable dissimilarity in the large negative tails of the probability density functions. The correlation results show that the streamwise extent of the WSS fluctuations becomes smaller, in contrast to that of the WHF fluctuations, and a considerable decrease in the convection velocity is observed downstream from the curvature. It is found that the curvature qualitatively modifies the WHF frequency spectra, leading to a shift to lower frequencies, while the spectral alternation is less pronounced for the WSS. Importantly, the mean WHF and WSS are also decomposed into different physically informed components, with the finding that the mean WSS generation is fundamentally changed by the curvature but the generation mechanism of the mean WHF is constant throughout the concave surface. Finally, an analysis of velocity and temperature structures is performed with the aid of bidimensional empirical mode decomposition to quantitatively demonstrate the contributions of specific spanwise length scales. We highlight that the outer large-scale organized structures, which are significantly energized by the concave surface, make an increasingly important contribution to the mean WSS and WHF generation.

DOI: [10.1103/PhysRevFluids.8.124602](https://doi.org/10.1103/PhysRevFluids.8.124602)

### I. INTRODUCTION

Compressible turbulent boundary layers (TBLs) over concave surface curvature are of major interest in the design of high-speed aircraft and propulsion systems, such as airfoils, turbine blades, and combustion chambers. It is now well established that the presence of concave surface curvature destabilizes a boundary layer [1–3], leading to an enhancement in turbulent mixing [2] and an increase in wall skin friction [3]. The response of a compressible TBL in such a flow is associated with the simultaneous action of concave streamline curvature, an adverse pressure gradient (APG), and bulk compression, which were originally defined as extra strain rates by Bradshaw [1], in

\*Corresponding author: [yuanxianxu@cardc.cn](mailto:yuanxianxu@cardc.cn)

addition to the mean shear. Despite the development of some general conclusions in the past few decades, as reviewed by Smits [2] and Spina *et al.* [3], the kinematic and dynamic behaviors involved in incompressible concave boundary layers are not yet fully understood due to the flow complexity, and there is still a clear need to investigate the influence of these extra strain rates on boundary layer turbulence, both separately and in combination.

Most previous studies related to concave-curvature compressible TBLs have been experimental and confined to mean-flow and turbulence behaviors. For instance, Sturek and Danberg [4,5] observed a logarithmic region in the mean velocity profiles of a supersonic APG boundary layer along an isentropic curved ramp model. This observation was inconsistent with measurements obtained by Laderman [6], who found that the distorted velocity profiles obviously deviated from the logarithmic law and explained this deviation through an increase in the mixing length. Later, Jayaram *et al.* [7] measured turbulent fluctuations inside a supersonic TBL over short regions of concave surface curvature with two different curvature radii (equal to 10 and 50 initial boundary layer thicknesses) and made a comparison with the corresponding  $8^\circ$  corner flow. It was revealed that increasing the curvature radius led to larger amplification of the absolute turbulent stresses, whereas the structural parameters were essentially unchanged. The authors argued that the rapid perturbations in the short radius model are characterized by the total strains and insensitive to the path taken, while the local strain rates are more pronounced in the large radius model. However, no unsteady longitudinal roll cells were observed in the above-cited supersonic experiments, in contrast to the generation of Taylor-Görtler type vortices previously discussed by Bradshaw [1] and Hoffmann *et al.* [8] in subsonic concave flows. Donovan *et al.* [9] further investigated the response of large-scale motions in a TBL at Mach 2.86 to a short region of strong concave surface curvature. They found that the combined effect of all the extra strain rates was to increase the characteristic structure angles and double the streamwise extent of the average large-scale motions. Neel *et al.* [10] examined the effects of a streamline curvature-induced APG on a Mach 4.9 TBL using quadrant decomposition analysis. They reported that the amplified Reynolds shear stress can be attributed to the corresponding increase in the magnitude and percentage of Q2 and Q4 events in the near-wall region, reflecting essential changes in the near-wall-flow structures. Wang *et al.* [11,12] carried out an experimental campaign on the structural responses of a Mach 2.95 TBL to different concave curvatures. Collectively, high-resolution measurements based on nanoparticle-based planar laser scattering and particle image velocimetry revealed that the upstream large-scale vortices appeared to break up into smaller ones in the concave region and that this was more pronounced for a larger curvature. The authors suggested that the increased turbulence level was brought about by statistically well-organized hairpin packets, which were significantly reinforced by the concave curvature.

Although only a very limited number of experiments designed to study the extra strain rates separately have been reported so far, significant progress has already been made in understanding the separate contributions of concave streamline curvature and APGs. In remarkable work by Thomann [13], the pressure gradient along a concave wall was eliminated by fitting suitably shaped bodies opposite the test surface to investigate the influence of streamwise wall curvature alone on heat transfer. They noted that the rate of heat transfer increased by about 20% due to the wall curvature. In another example, Fernando and Smits [14] performed experiments on a flat-plate supersonic turbulent boundary layer imposed by a reflected wave system and found that the obtained mean wall pressure distribution matched that of the supersonic curved-wall model previously studied by Jayaram *et al.* [7]. Their quantitative comparisons suggested that the increases in the wall friction for the curved-wall experiments were only around 17% larger than that in the flat-plate case, and the additional effect of concave streamline curvature on the Reynolds stress field was more significant than on the mean velocity profiles. Similar companion experiments were also conducted by Smith and Smits [15], who pointed out that the destabilizing effect of the bulk compression is generally complemented by the influence of concave curvature and that a larger curvature leads to a greater increase in the wall shear stress (WSS) and Reynolds stresses inside the disturbed boundary layer. Furthermore, Wang *et al.* [16] performed an experimental investigation on an APG flat plate and

a concave wall at Mach 2.95 using particle image velocimetry and suggested that the concave curvature (in the form of centrifugal instability) exhibits an influence on the boundary layer that is similar to that of an adverse pressure gradient.

Direct numerical simulation (DNS) has provided a powerful alternative tool with which to shed light on the evolution of compressible concave flows from the numerical perspective, since a well-resolved flow field with the full range of spatial and temporal scales of turbulence cannot possibly be measured in experiments. A preliminary attempt to perform a DNS study of a supersonic concavely curved flow was undertaken by the present authors [17]. The response of a turbulent boundary layer at  $M_\infty = 2.9$ ,  $Re_\theta = 2300$  to a curved compression ramp with a total turning angle of  $24^\circ$  and a radius of curvature  $R = 15\delta$  (with  $\delta$  being the initial boundary layer thickness) was analyzed. The presence of unsteady longitudinal roll cells, which were not observed in previous experiments, was highlighted. A dynamic mode decomposition analysis of the streamwise velocity fields in the spanwise-wall-normal plane also showed a qualitative association between the dominant low-frequency dynamic modes and the Görtler-like vortices.

Sun *et al.* [18] carried out DNS studies of supersonic Mach 2.7 flows over concave surfaces with two different curvature radii to comparatively investigate the effect of concave curvature on turbulence structures and statistics. They noted that Görtler-like vortices generated by the significant centrifugal effects occurred in the outer region of the boundary layer, while abundant small-scale vortices on the concave wall were associated with baroclinic production from the interaction of the density gradients and concave compression. They also showed that compressibility effects in the concave case with a large curvature rate were not negligible and that the profiles of the turbulent kinetic energy and turbulent Mach number were featured by a characteristic two-layer structure. In follow-up work, Wang *et al.* [19] analyzed the amplification of large-scale motions in a supersonic concave boundary layer and its impact on mean properties and turbulence statistics. It was found that the interaction between low- and high-momentum flows was significantly promoted by the large-scale streamwise roll cells, especially in the outer layer, and a large number of hairpin vortices were generated in the near-wall region, resulting in a stronger wall-normal correlation. Similarly, the DNS data of Wu *et al.* [20] showed that the striking amplification of outer-layer turbulence, as evidenced by energy spectra, was mainly contributed by the increasingly energized large-scale motions in the outer boundary layer. By inspecting the spanwise two-point correlations, they quantified the amplitude modulation of the inner-outer interactions and demonstrated that the considerably enhanced turbulence modulation caused by the concave surface was still governed by logarithmic-region superstructures, rather than the large-scale motions in the lower-wake region. In a more recent DNS of hypersonic APG TBLs over a planar concave wall, Nicholson *et al.* [21] showed that the pressure gradient had little effect on the turbulent Prandtl number and the modified strong Reynolds analogy, whereas profiles of turbulence intensities at different pressure gradients did not collapse under Morkovin's scaling.

The aim of the present study is to investigate the behaviors of the WSS and wall heat flux (WHF) in concave-curvature flows, which are still not well understood. To our knowledge, except for the DNS study of wall pressure fluctuations given by Sun *et al.* [18], direct measurement and numerical analysis of the wall-flow variables with concave surface have been mainly paid on the mean distribution; the current paper is an attempt to make the best of DNS to uncover the combined effect of all the extra strain rates on the WSS and WHF fluctuations, which provides absolute access to the whole fluctuating fields that are very difficult to obtain in experiments. As far as the mean wall quantities are concerned, how the changes in turbulence structures relate to the generation of the mean WSS and WHF is still unknown. The objective of this work is to fill in the above gaps by delineating a statistical picture of the fluctuating WSS and WHF, including the probability density function (PDF), space-time correlations, and power spectra, and by decomposing the mean wall-flow variables into physics-informed contributions using the identities proposed by Li *et al.* [22] and Sun *et al.* [23]. In the cases of wall-bounded boundary layer flows [24–26] and the interaction of impinging shock waves with TBLs [27–29], the quantitative contributions of various turbulent scales to the mean WSS and WHF have been identified using these novel theoretical

decompositions, with the aid of the bidimensional empirical mode decomposition (BEMD) method. These investigations inspire us to adopt a similar methodology to explore the underlying generation mechanisms in supersonic concave TBLs.

In this paper, a new DNS is performed of a TBL with a Mach number of  $M_\infty = 2.25$  and a friction Reynolds number of  $Re_\tau = 769$  subjected to a longitudinal concave surface with a total turning angle of  $24^\circ$ . The radius of curvature is 20 initial boundary layer thicknesses. The major consideration for the inflow conditions and concave curvature selected is to make sure that the shock wave is formed just outside the boundary layer, and therefore, that a smooth rise in pressure is generated throughout the concave surface, as in the previous experiments of Jayaram *et al.* [7] and Donovan *et al.* [9]. The setup of the simulation is briefly introduced in Sec. II, together with a validation of the DNS data. In Sec. III, the general properties of the flow field, key statistical results, and decomposition analysis are discussed. Finally, the concluding remarks are given in Sec. IV.

## II. SIMULATION SETUP

### A. Numerical strategy

We solve the three-dimensional compressible conservative Navier-Stokes equations, nondimensionalized by the inflow parameters, for a perfect gas with a ratio of specific heat  $\gamma = 1.4$  and a Prandtl number  $Pr = 0.71$ . The pressure  $p$ , density  $\rho$ , and temperature  $T$  are assumed to obey the ideal-gas equation of state, and the Sutherland law is adopted to calculate the molecular viscosity  $\mu$ . The thermal conductivity is calculated as  $k = \mu C_p / Pr$ , with the heat capacity at constant pressure being  $C_p = 1/(\gamma - 1) M_\infty^2$ . Details of these equations are provided in the work of Tong *et al.* [17]. The present DNS is performed using an open-source code OpenCFD-SC, provided by Li *et al.* [30,31]. This high-order finite difference flow solver has been extensively used to simulate a wide range of shock-induced separated flows [32,33] and hypersonic transitional boundary layers [34,35]. The discretization of the adopted governing equations is fulfilled by a bandwidth-optimized fourth-order weighted essentially nonoscillatory scheme [36] with Steger-Warming flux splitting for the inviscid fluxes, an eighth-order accurate central difference scheme for the viscous fluxes, and a third-order total variation diminishing Runge-Kutta method [37] for the time integration. The freestream Mach number, static temperature, and unit Reynolds number are  $M_\infty = 2.25$ ,  $T_\infty = 169.44$  K, and  $Re_\infty/\text{mm} = 2.5 \times 10^4$ , in accordance with recent DNS studies by Tong *et al.* [25]. Throughout this paper, the subscript “ $\infty$ ” indicates that the quantity is taken in the freestream, while the subscript “w” represents a quantity at the wall.

In the present study, a turbulent boundary layer is initially developed on a zero-pressure-gradient flat plate before entering a curved surface region with a total turning angle of  $24^\circ$  and then relaxing on a flat plate downstream. The overall size of the computational domain sketched in Fig. 1 is  $L_x \times L_y \times L_z = 87.7\delta \times 14.0\delta \times 5.0\delta$  in the direction along the bottom wall ( $x$ ), in the direction normal to the bottom wall ( $y$ ), and in the spanwise direction ( $z$ ), respectively, with  $\delta = 1.27$  mm being the nominal thickness of the incoming turbulent boundary layer at the reference location  $x_{\text{ref}}$ , estimated hereafter from the 99% freestream velocity. In the following,  $\delta$  denotes the boundary layer thickness at  $x_{\text{ref}}$ ;  $x$ ,  $y$ , and  $z$  are the body intrinsic coordinates in the local tangential, wall-normal, and spanwise directions, respectively; and  $u$ ,  $v$ , and  $w$  are the corresponding velocity components. Meanwhile,  $X$ ,  $Y$ , and  $Z$  refer to the Cartesian coordinates, and  $U$ ,  $V$ , and  $W$  are the velocity components in the axial, transverse, and spanwise directions, respectively. The origin  $(x, y) = (0, 0)$  is located at the start of the curvature  $X_s$ , having the same origin as  $X$  and  $Y$ . The domain inlet and the reference location  $x_{\text{ref}}$  are placed at  $X = -56.0\delta$  and  $X = -5.5\delta$ , respectively, and the curvature ends at  $X_e = 8.8\delta$ . A region of blowing and suction, as shown by the contour of the instantaneous velocity  $V/U_\infty$ , is centered at the bottom wall between  $X_a = -50.0\delta$  and  $X_b = -40.0\delta$  to induce the laminar-to-turbulent transition, which generates the fully developed TBL upstream of the curved region, as illustrated by the contour of instantaneous velocity  $U/U_\infty$  in the  $X$ - $Y$  plane at  $Z = 0$ .

The grid spacing in the spanwise direction is uniform and the grid points in the  $X$ - $Y$  plane are sketched in Fig. 2. In the streamwise direction, the grid points are equally distributed in the region

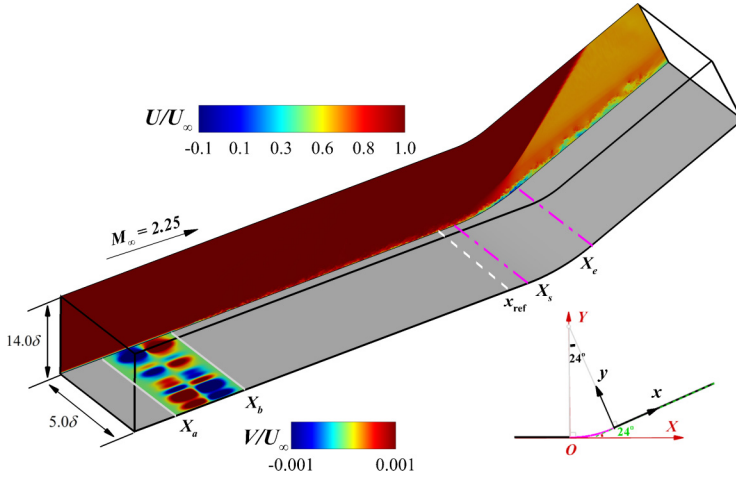


FIG. 1. A sketch of the computational domain together with the contour of the instantaneous velocity  $U/U_\infty$  in the  $X$ - $Y$  plane at  $Z = 0$  and the contour of the instantaneous velocity  $V/U_\infty$  at the wall in the blowing and suction region located between  $X_a$  and  $X_b$ . The variables  $X_s$  and  $X_e$  denote the start and end points of the curved region, respectively. The reference location is denoted by  $x_{\text{ref}}$ . The inset shows a side view of the curved region.

of interest between  $x = -16.0\delta$  and  $x = 27.0\delta$ , while the grid spacing is progressively refined in the transition zone at  $x < -16.0\delta$  and is sharply coarsened in the fringe zone at  $x > 27.0\delta$ . In the wall-normal direction, grid stretching is used to guarantee that there are at least 280 points clustered inside the boundary layer to adequately resolve turbulent structures. In our simulations, two grids with different resolutions are considered, denoted Grid A ( $n_x \times n_y \times n_z = 3094 \times 430 \times 340$ ) and Grid B ( $n_x \times n_y \times n_z = 4244 \times 430 \times 485$ ). For both grids, the grid resolutions in the wall-normal direction are nearly the same, with  $\Delta y_w^+ = 0.55$  (the first grid point from the wall) and  $\Delta y_e^+ = 8.0$  (at the boundary layer edge), respectively. Going from Grid A to Grid B, the streamwise and spanwise grid spacing in the well-resolved curvature region are decreased from  $\Delta x^+ = 11.4$  and  $\Delta z^+ = 9.9$  to  $\Delta x^+ = 8.2$  and  $\Delta z^+ = 7.1$ , respectively. The present computational grid resolutions are comparable to the values adopted in well-accepted DNS studies of compressible turbulent wall-bounded flows [38,39]. Unless otherwise stated, the subscript “+” stands for a quantity scaled in wall units at  $x_{\text{ref}}$ .

To generate the inflow turbulence, a steady laminar boundary layer profile provided by Tong *et al.* [25] is applied at the domain inlet, and the normal velocity disturbances proposed by Pirozzoli *et al.* [40], including two temporal modes, two spatial modes in the streamwise direction, and ten spatial modes in the spanwise direction, are applied in the wall blowing and suction region with

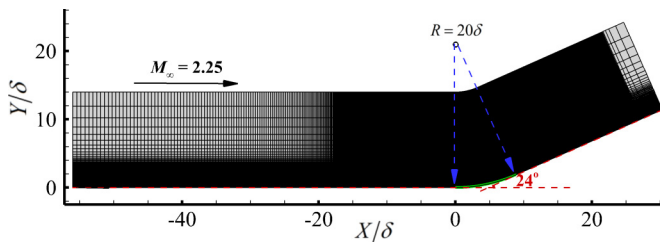


FIG. 2. A sketch of the computational grid in the  $X$ - $Y$  plane. The grid points are displayed every three points in both directions.

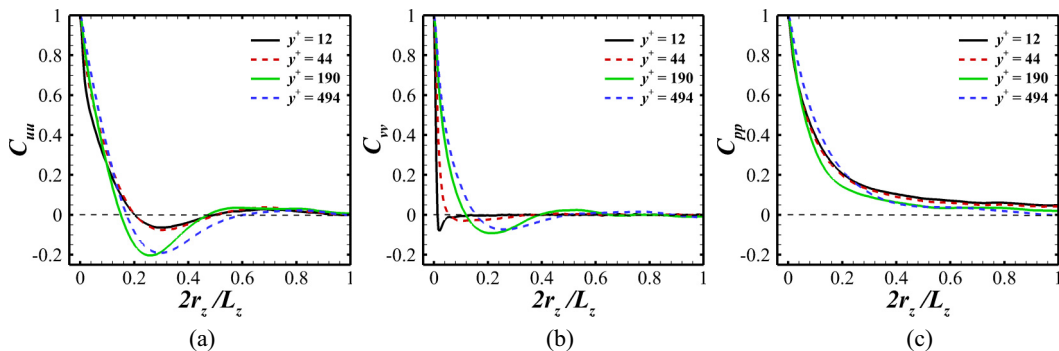


FIG. 3. Spanwise two-point correlation coefficients at  $X/\delta = 8.0$ : (a) streamwise velocity  $C_{uu}$ ; (b) wall-normal velocity  $C_{vv}$ ; (c) pressure  $C_{pp}$ .

a net flow rate of zero. The selected disturbance amplitude and fundamental frequency, which are the same as those used by Tong *et al.* [25–28], produce a realistic turbulent boundary layer after the transition within a short distance of about 125 times the inflow boundary layer thickness. Note that the grid is sharply coarsened to drive the flow toward a uniform state in the fringe region, and supersonic outflow boundary conditions are applied at the domain outlet. Additionally, no-slip isothermal conditions are enforced at the bottom wall, while nonreflecting conditions are enforced at the parallel top boundary layer to eliminate the reflection of disturbances back into the domain. The constant wall temperature is  $T_w = 254.16$  K, corresponding to 0.75 times the recovery temperature  $T_r$ , and thus the wall is cold in the present study. In the span, the selected domain width is large enough to allow flow homogeneity (as discussed below) and periodic boundary conditions are imposed on both sides.

We start the simulations by using the imposed laminar boundary layer profile at the domain inlet to initialize the full three-dimensional flow field and perform flow sample collection for a time period of approximately  $500\delta/U_\infty$  when the effect of the initial transient flow is washed out after a time period of about  $170\delta/U_\infty$ . In the results that follow, either Reynolds or Favre averaging is used for a generic variable  $\phi$ . The Reynolds average  $\phi$  over the spanwise direction and time is denoted by  $\langle\phi\rangle$  or  $\bar{\phi}$ , while the Favre average is denoted by  $\{\phi\} = \langle\rho\phi\rangle/\langle\rho\rangle$  or  $\bar{\phi} = \bar{\rho}\bar{\phi}/\bar{\rho}$ . The corresponding fluctuations are then obtained as  $\phi' = \phi - \langle\phi\rangle$  and  $\phi'' = \phi - \{\phi\}$ , respectively.

## B. Numerical validity

Assessments of the domain width are performed in Fig. 3, where spanwise two-point correlation coefficients for the velocity and pressure fluctuations at  $X/\delta = 8.0$  are plotted as computed on Grid B. For the four wall-normal locations selected (from the near-wall region to the outer region), all the correlations confirm that the turbulent fluctuations are uncorrelated as the spanwise separation  $r_z$  is over  $L_z/2$ , suggesting that the domain width used is large enough and the turbulence dynamics inside the curved region are not inhibited. Similar results (not shown here for clarity) can be obtained at other streamwise locations.

The accuracy of the inflow turbulence is assessed by examining the mean-flow properties and turbulence statistics at the reference location  $x_{\text{ref}}$  computed on Grid B. In Fig. 4(a), the obtained shape factor  $H_{12}$  is compared with the empirical relation given by Hopkins *et al.* [41] and the DNS data reported by Huang *et al.* [42], and good agreement is seen. The wall-normal profile of the van Driest transformed mean streamwise velocity  $\langle u_{\text{vd}} \rangle^+$ , shown in Fig. 4(b), agrees very well with the compressible DNS data for zero-pressure-gradient TBLs given by Tong *et al.* [25] and Fang *et al.* [43] under similar flow conditions. Clearly, the well-resolved viscous sublayer at  $y^+ < 6$  and the logarithmic region at  $30 < y^+ < 100$  obey the classic law of the wall, consistent with

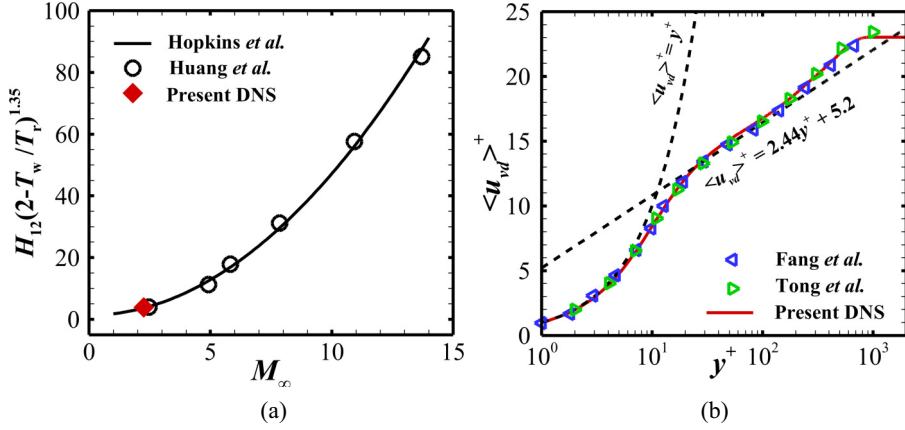


FIG. 4. Mean-flow properties at the reference location  $x_{\text{ref}}$ : (a) shape factor  $H_{12}$ ; (b) profile of the van Driest transformed mean streamwise velocity  $\langle u_{\text{vd}} \rangle^+$ .

canonical wall-bounded turbulent flow structures. The high resolution in the present simulation is further confirmed in Fig. 5(a), where the wall-normal profiles of the density-scaled Reynolds stress components  $R_{ij}$  normalized by the square of the friction velocity  $u_\tau$  agree well with the numerical results of Fang *et al.* [43] and the experimental measurements of Eléna and Lacharme [44] at  $M = 2.23$  and  $\text{Re}_\theta = 4700$ . In addition, the computed temperature-velocity correlation coefficient,  $R_{uT}$ , plotted in Fig. 5(b), with an approximate value of 0.55 at  $y/\delta > 0.2$ , exhibits close similarities with those in the DNS database of Pirozzoli and Bernardini [38] with  $\text{Re}_\tau = 1116$  at  $M = 2.0$  and Huang *et al.* [42] with  $\text{Re}_\tau = 774$  at  $M = 2.5$  and 4.9. This ensures that a fully developed equilibrium state of the incoming TBL is obtained at the reference location upstream of the concave curvature.

The sensitivity of the numerical results to the grid resolution is investigated by comparing the time- and spanwise-averaged wall quantities as well as root-mean-square (rms) values computed from the two grids. In Fig. 6, the spatial distribution of wall pressure, skin friction coefficient, and heat flux is shown, respectively. Across the concave curvature, the wall pressure and heat flux increase smoothly, while the skin friction coefficient drops and no mean-flow separation occurs.

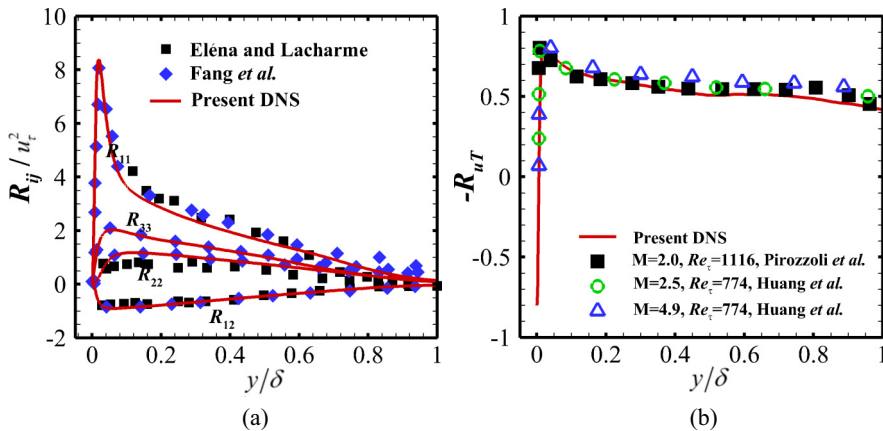


FIG. 5. Turbulence statistics at the reference location  $x_{\text{ref}}$ : (a) density-scaled Reynolds stress components  $R_{ij} = \langle (\rho)/\langle \rho_w \rangle \{u_i' u_j'\}$ ; (b) temperature-velocity correlation coefficient,  $R_{uT}$ .

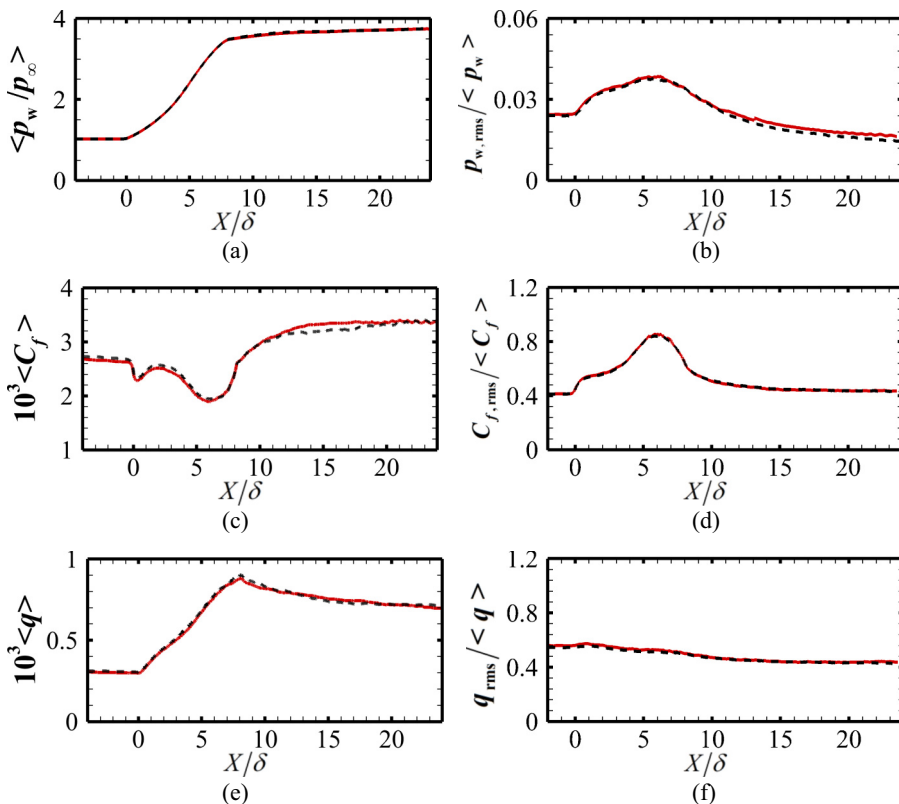


FIG. 6. Distribution of time- and spanwise-averaged (left) and root-mean-square (right) wall quantities for both grids: (a) pressure; (b) skin friction coefficient; (c) heat flux. Red: Grid A; black: Grid B.

Going from Grid A to Grid B, all the curves nearly collapse, with the notable differences being less than 5% seen in Fig. 6(c). It can be concluded that the present resolution is adequate to obtain grid-converged results. Thus, the analysis given below is based on results calculated using Grid B.

### III. RESULTS AND DISCUSSION

#### A. General properties of the flow field

The instantaneous temperature field in the  $X$ - $Y$  midplane presented in Fig. 7(a) gives a first impression of the flow characteristics in the concave region. As expected, the curvature diffuses the shock wave into a weak compression fan near the boundary layer edge in a qualitatively similar way to that seen in the schlieren photograph experiments performed by Donovan *et al.* [9] for turbulent flows over a  $16^\circ$  concave surface curvature. Across the curvature, the temperature significantly increases and the boundary layer thickness becomes thinner at  $0 < X/\delta < 6$ , followed by an obvious thickening in the downstream relaxation. Another important observation is clearly seen in Figs. 7(b)–7(d), where three cross-sectional planes at  $X/\delta = 0$  (the start of the curvature), 8.0 (almost the end of the curvature), and 20.0 (far downstream from the curvature) are shown, respectively. In Fig. 7(b), the upstream TBL is characterized by high-temperature fluids in the near-wall region and highly intermittent low-temperature turbulent bulges in the outer layer, which resemble those found in previous studies of wall-bounded turbulent flows [38,40]. Meanwhile, the  $\delta$ -sized high-temperature bulges in the outer region of the distorted boundary layer [see Figs. 7(c) and 7(d)] imply the existence of large-scale longitudinal roll cells. Similar behavior of the enhanced

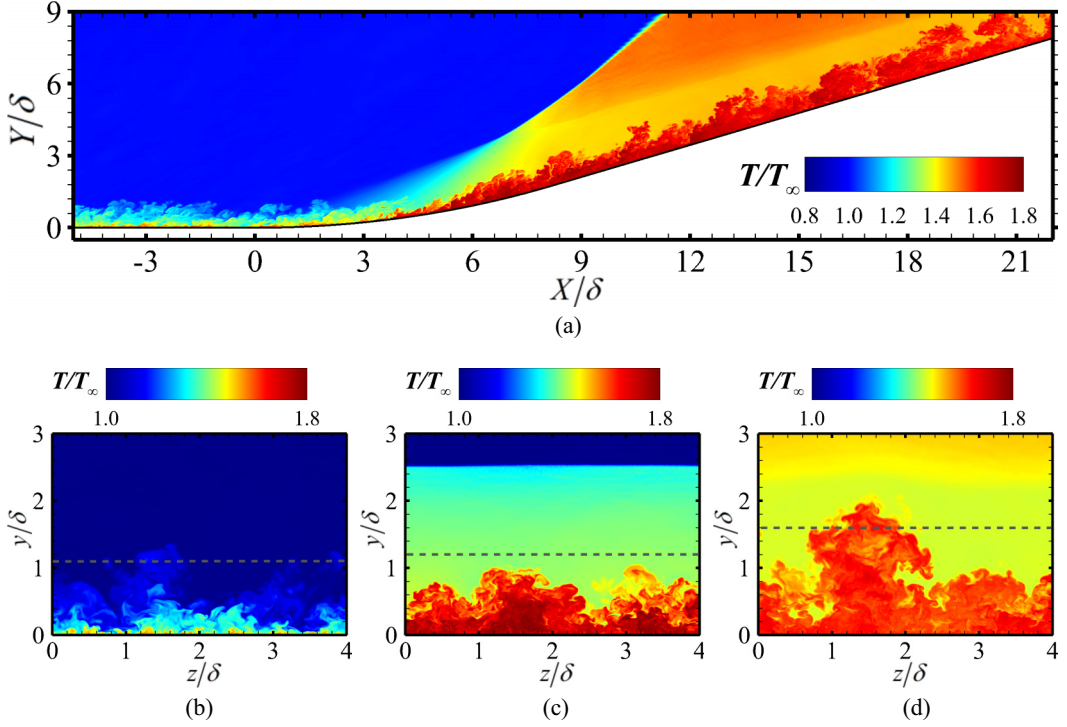


FIG. 7. Contours of the instantaneous temperature field  $T/T_\infty$ : (a)  $X$ - $Y$  midplane; (b)  $y$ - $z$  plane at  $X/\delta = 0$ ; (c)  $y$ - $z$  plane at  $X/\delta = 8.0$ ; (d)  $y$ - $z$  plane at  $X/\delta = 20$ . The dashed lines in (b)–(d) denote the local boundary layer thickness.

momentum transport in a concave turbulent boundary layer DNS was also reported by Wang *et al.* [19] at a turning angle of  $12^\circ$ .

To give a three-dimensional representation of the flow, in Fig. 8 we visualize the instantaneous vortex structures in terms of the isosurface of the  $Q$  criterion [45]. The figure highlights an augmentation of the outer-layer vortices after the flow passes through the weak compression fan and relaxes in the downstream region, which is consistent with the occurrence of the outer energetic peaks in the spanwise energy spectra (as discussed below). These amplified vortices, frequently seen at  $X/\delta > 5$ , appear to be organized into large-scale coherent structures in the outer region, with a streamwise length scale  $O(10\delta)$ . Such behavior in vortical activity is likely associated with Görtler-like structures, which are difficult to distinguishably extract from turbulent flows, as previously explained by Sun *et al.* [18] for the case of supersonic concave surface curvature.

The contours of the time-averaged WSS and WHF fields are shown in Figs. 9(a) and 9(c), respectively, while the instantaneous WSS and WHF fluctuations, calculated as

$$\tau'(X, Z, t) = \tau - \langle \tau \rangle = \mu \left. \frac{\partial u(X, y, Z, t)}{\partial y} \right|_w - \left\langle \mu \left. \frac{\partial u(X, y, Z, t)}{\partial y} \right|_w \right\rangle, \quad (1)$$

$$q'(X, Z, t) = q - \langle q \rangle = k \left. \frac{\partial T(X, y, Z, t)}{\partial y} \right|_w - \left\langle k \left. \frac{\partial T(X, y, Z, t)}{\partial y} \right|_w \right\rangle \quad (2)$$

are shown in Figs. 9(b) and 9(d), respectively. It is apparently seen that both the time-averaged WSS and WHF fields exhibit significant variations in the spanwise direction at  $X/\delta > 0$ , implying a strong spanwise modulation inside the curved region. Similar findings of the time-averaged WSS in sharp compression ramp simulations were also reported by Grilli *et al.* [46] and Loginov *et al.*

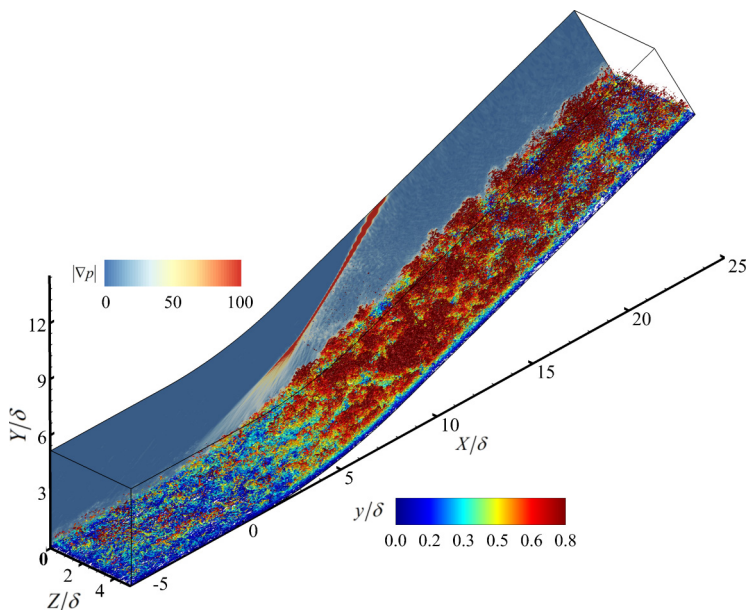


FIG. 8. The instantaneous vortex structure extracted using the  $Q$  criterion, colored with the wall-normal distance and contour of the pressure gradient modulus in the  $X$ - $Y$  plane at  $Z = 0$ . The isosurface of  $Q$  equalling to 0.2% of its global maximum is shown.

[47], who explained the spanwise variations as footprints of counter-rotating steady streamwise vortices. It is important to note that the mean flow is attached, but small patches of  $C_f < 0$  reveal instantaneous flow reversal occurring in the curvature [see the black solid lines in Figs. 9(b) and 9(d)]. The maximum statistical probability of negative skin friction is below 8% at  $X/\delta = 5.6$ , indicating that the flow is in the incipient detachment state, as suggested by Simpson [48]. As

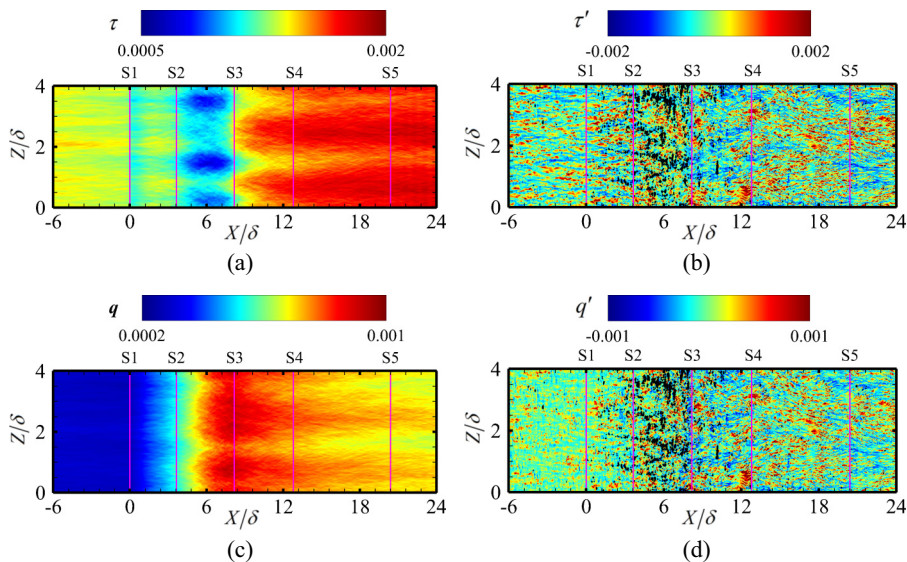


FIG. 9. Contours of time-averaged fields (left) and instantaneous fluctuations (right) with the isoline  $C_f = 0$  in black: (a), (b) WSS; (c), (d) WHF. The solid lines denote five streamwise locations S1–S5.

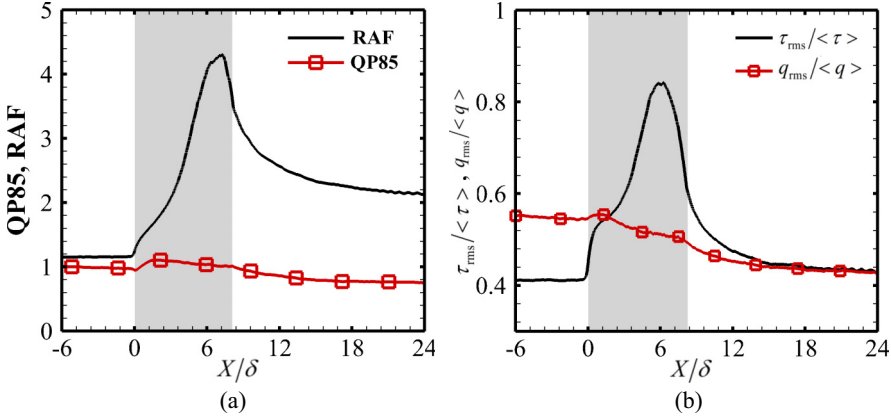


FIG. 10. (a) A comparison of the Reynolds analogy factor and QP85 scaling; (b) the streamwise variation of the root-mean-square level of the WSS and WHF fluctuations normalized by the local mean values,  $\langle \tau \rangle$  and  $\langle q \rangle$ . The shaded areas in (a) and (b) denote the concave surface.

anticipated for TBLs [25], both the WSS and the WHF fluctuations are streamwise elongated, and the characteristic length scales of the former are much larger than those of the latter. It is seen that the predominance of streamwise coherence is still maintained in the curved region with a locally reversed flow. More interestingly, there are increasingly pronounced similarities between  $\tau'$  and  $q'$  downstream from the curvature at  $X/\delta > 8.0$ , except for the notable differences in magnitude. These qualitative observations of the fluctuating WSS and WHF fields will be extended and clarified in the next few sections, in which the statistical behaviors of  $\tau'$  and  $q'$  at six different streamwise locations ( $x_{\text{ref}}$  and S1–S5) will be investigated through a comparative analysis. Here three locations denoted as S1–S3 are placed at the onset, midpoint, and endpoint of the curvature, respectively, and two locations denoted as S4 and S5 are placed at  $X/\delta = 12.8$  and  $20.4$  in the downstream relaxation region, respectively.

Figure 10(a) compares the streamwise distribution of the Reynolds analogy factor (RAF) and QP85 scaling, which are defined as  $\text{RAF} = 2\langle q \rangle / \langle C_f \rangle$  and  $\text{QP85} = (\langle q \rangle / \langle q \rangle_u) (\langle p_w \rangle_u / \langle p_w \rangle)^{0.85}$ , respectively, with  $\langle q \rangle_u$  and  $\langle p_w \rangle_u$  being the mean WHF and wall pressure at the reference location  $x_{\text{ref}}$ . Upstream of the curvature, the RAF and QP85 are nearly constant, with  $\text{RAF} \approx 1.15$  and  $\text{QP85} \approx 0.98$ , in good agreement with the hypersonic boundary layer simulations of Priebe and Martin [39], who reported  $\text{RAF} \approx 1.2$  and  $\text{QP85} \approx 1.0$  for  $\text{Re}_\theta = 3300$ . It can be seen that the RAF experiences a rapid increase in the concave region, attaining a peak value of  $\text{RAF} \approx 4.28$  at  $X/\delta \approx 7.2$ , and then undergoes a slow decrease in the downstream relaxation region, approaching  $\text{RAF} \approx 2.15$  at  $X/\delta = 24$ . Meanwhile, the value of QP85 is relatively unchanged by the curvature, and varies between 0.76 and 1.10, supporting the validity of the scaling linking the mean WHF and wall pressure in the concave boundary layer. Moreover, the root-mean-square fluctuations in the WSS and WHF ( $\tau_{\text{rms}}$  and  $q_{\text{rms}}$ ) are displayed in Fig. 10(b) as functions of  $X/\delta$ , where the intensities are normalized by the local mean values,  $\langle \tau \rangle$  and  $\langle q \rangle$ , respectively. At  $X/\delta < 0$ ,  $\tau_{\text{rms}}/\langle \tau \rangle$  attains a constant value of 0.411, which matches the incompressible empirical correlation proposed by Örlü and Schlatter [49],  $\tau_{\text{rms}}/\langle \tau \rangle = 0.298 + 0.018 \ln \text{Re}_\tau$ , and the fluctuation amplitude in the WHF exhibits a larger fraction of the mean value, where  $q_{\text{rms}}/\langle q \rangle \approx 0.55$ , very close to the typical values reported by Huang *et al.* [42] for hypersonic cold-wall TBLs under various flow conditions. Notably, the overall trends of  $\tau_{\text{rms}}/\langle \tau \rangle$  and  $q_{\text{rms}}/\langle q \rangle$  are completely different on the concave surface, which is primarily due to the difference in the respective mean value, but the scaled WSS and WHF fluctuations are nearly equal, attaining an approximate value of 0.431 in the relaxation region at  $X/\delta > 16$ , implying that the recovery of the fluctuating WSS is much faster than that of the fluctuating WHF.

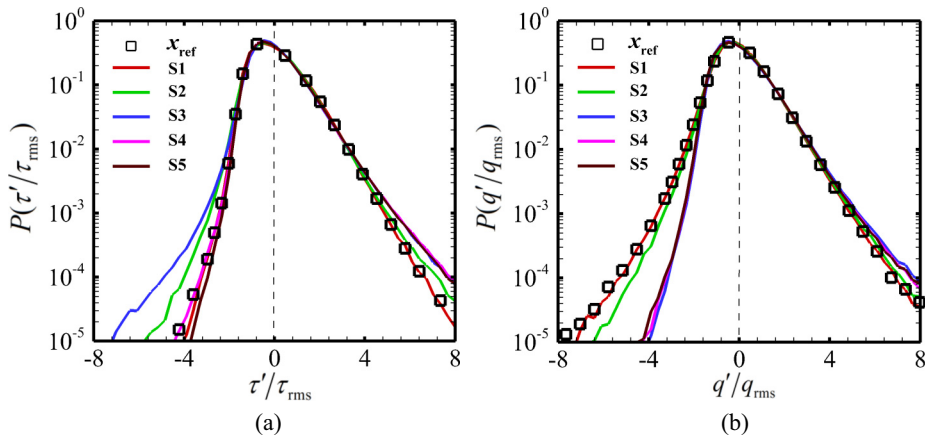


FIG. 11. PDFs of the fluctuating WSS and WHF at various streamwise locations: (a)  $P(\tau'/\tau_{\text{rms}})$ ; (b)  $P(q'/q_{\text{rms}})$ .

### B. Probability density function

The PDFs of the WSS and WHF fluctuations at various streamwise locations are shown in Fig. 11. It is clearly seen from the figure that all of the PDFs exhibit a skewed behavior for  $\tau'$  and  $q'$ , with the peaks occurring at  $\tau' \approx -0.5\tau_{\text{rms}}$  and  $q' \approx -0.5q_{\text{rms}}$ , respectively, as found by Yu *et al.* [50] in their compressible wall-bounded turbulence studies, but clear curvature dependence is observed for both the negative and the positive tails of the PDFs. That is, in the positive tail, the values slightly increase in the region S1–S2 and then collapse onto each other at S3–S5, indicating a higher occurrence probability of rare extreme events at  $\tau'/\tau_{\text{rms}} > 4$  and  $q'/q_{\text{rms}} > 4$ . In the negative tail, the influence of the curvature on  $\tau'$  and  $q'$  is different. A comparison of Figs. 11(a) and 11(b) highlights a significantly increased probability of extreme negative events at  $\tau'/\tau_{\text{rms}} < -4$  and a sharply decreased probability of extreme negative events at  $q'/q_{\text{rms}} < -4$ , since the PDFs of  $\tau'$  in the region S2–S3 become wider and the corresponding PDFs of  $q'$  become narrower. This dissimilarity is noteworthy due to the enhanced instantaneous separation flows along the concave surface (see Fig. 9). In addition, a faster recovery of the negative tails of  $\tau'$  is achieved in the relaxation region; that is, the PDFs at S4–S5 deviate slightly from the upstream profile, whereas the PDFs of  $q'$  show far lower values than those of  $x_{\text{ref}}$ .

In Fig. 12, the premultiplied PDFs are shown to investigate the fractional contributions of the rms values. As we can see, the dominant contribution of the positive fluctuations to  $q_{\text{rms}}$  and  $\tau_{\text{rms}}$  is very insensitive to the presence of curvature, with the main difference being a smaller amplitude at  $\tau'/\tau_{\text{rms}} \approx 1$ . Similar behavior was also found by Abe *et al.* [51], who studied the influence of the Reynolds number on surface heat flux fluctuations in low-speed turbulent channel flows up to  $\text{Re}_\tau = 1020$ . As expected, the effect of curvature is mainly reflected by the contributions of negative values to  $q_{\text{rms}}$  and  $\tau_{\text{rms}}$ . It is seen from Fig. 12(a) that the decreased contributions at  $\tau'/\tau_{\text{rms}} \approx -1$  are partially compensated for by a small increase in the contributions of extreme negative events of  $\tau'$ , whereas the local contributions at  $q'/q_{\text{rms}} \approx -1$  are increased to balance out the attenuated contributions at  $q'/q_{\text{rms}} < -2$ , as seen in Fig. 12(b).

The joint PDFs and premultiplied joint PDFs of the fluctuations of the WSS and WHF scaled by the local rms values ( $\tau_{\text{rms}}$  and  $q_{\text{rms}}$ ) at various streamwise locations, denoted as  $P(\tau', q')$  and  $\tau'q'P(\tau', q')$ , are plotted in Figs. 13(a) and 13(b), respectively, to examine the correlations between  $\tau'$  and  $q'$ . It is important to emphasize that the strong correlation is essentially not affected by the curvature, as evidenced by values of the correlation coefficient larger than 0.79 and the highly narrowed distributions of  $P(\tau', q')$ , with the major axis inclined in the first ( $\tau' > 0, q' > 0$ ) and third ( $\tau' < 0, q' < 0$ ) quadrants, as shown in Fig. 13(a). This behavior is better seen in Fig. 13(b),

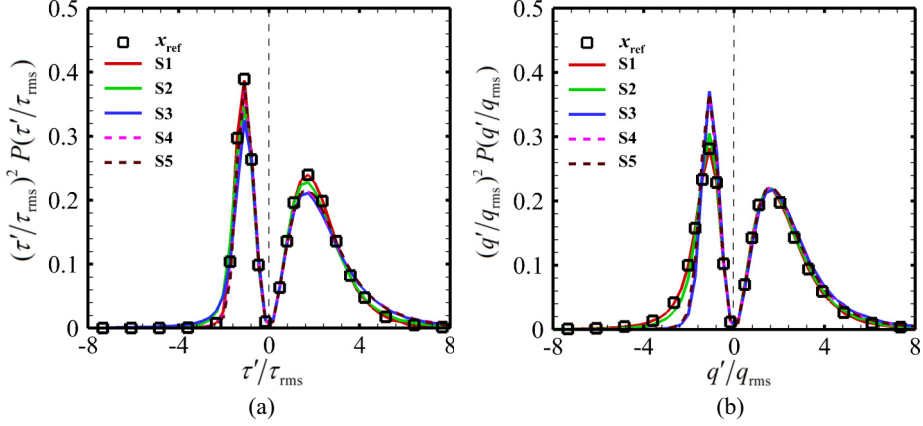


FIG. 12. Premultiplied PDFs of the fluctuating WSS and WHF at various streamwise locations: (a)  $(\tau'/\tau_{\text{rms}})^2 P(\tau'/\tau_{\text{rms}})$ ; (b)  $(q'/q_{\text{rms}})^2 P(q'/q_{\text{rms}})$ .

in which pairs of  $\tau'/\tau_{\text{rms}} \approx -1$  and  $q'/q_{\text{rms}} \approx -1$  contribute mostly to the observed high correlation coefficients at all the selected locations, in line with previous findings of Yu *et al.* [52].

### C. Space-time correlations

In this section, the influence of curvature on the structural properties of the WSS and WHF fluctuations is mainly investigated by comparing the two-point space-time correlation coefficients, computed as

$$R_{\tau\tau}(\Delta x^+, \Delta z^+, \Delta t^+) = \frac{\langle \tau'(x_0, z, t) \tau'(x_0 + \Delta x^+, z + \Delta z^+, t + \Delta t^+) \rangle}{\sqrt{\langle \tau'(x_0, z, t)^2 \rangle} \sqrt{\langle \tau'(x_0 + \Delta x^+, z + \Delta z^+, t + \Delta t^+)^2 \rangle}}, \quad (3)$$

$$R_{qq}(\Delta x^+, \Delta z^+, \Delta t^+) = \frac{\langle q'(x_0, z, t) q'(x_0 + \Delta x^+, z + \Delta z^+, t + \Delta t^+) \rangle}{\sqrt{\langle q'(x_0, z, t)^2 \rangle} \sqrt{\langle q'(x_0 + \Delta x^+, z + \Delta z^+, t + \Delta t^+)^2 \rangle}} \quad (4)$$

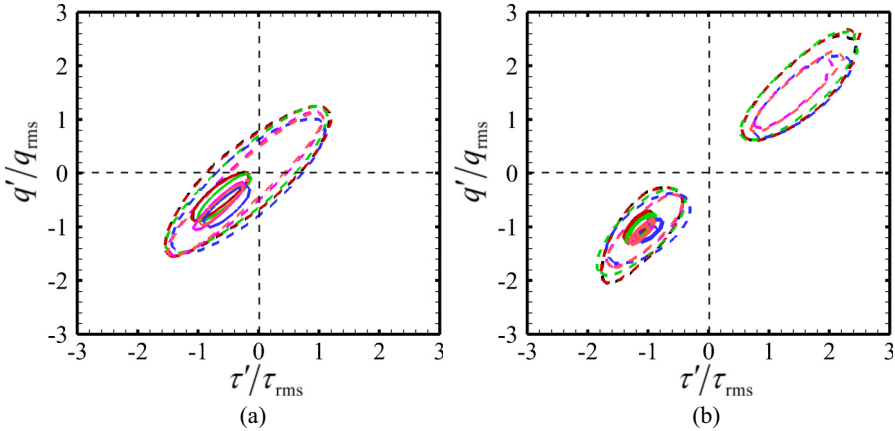


FIG. 13. Joint PDFs and premultiplied joint PDFs at various streamwise locations: (a)  $P(\tau'q')$ ; (b)  $\tau'q'P(\tau', q')$ . The solid and dashed contour lines correspond to 0.8 and 0.2 times the maximum value, respectively.  $x_{\text{ref}}$ : black; S1–S5: red, green, blue, pink, and orange.

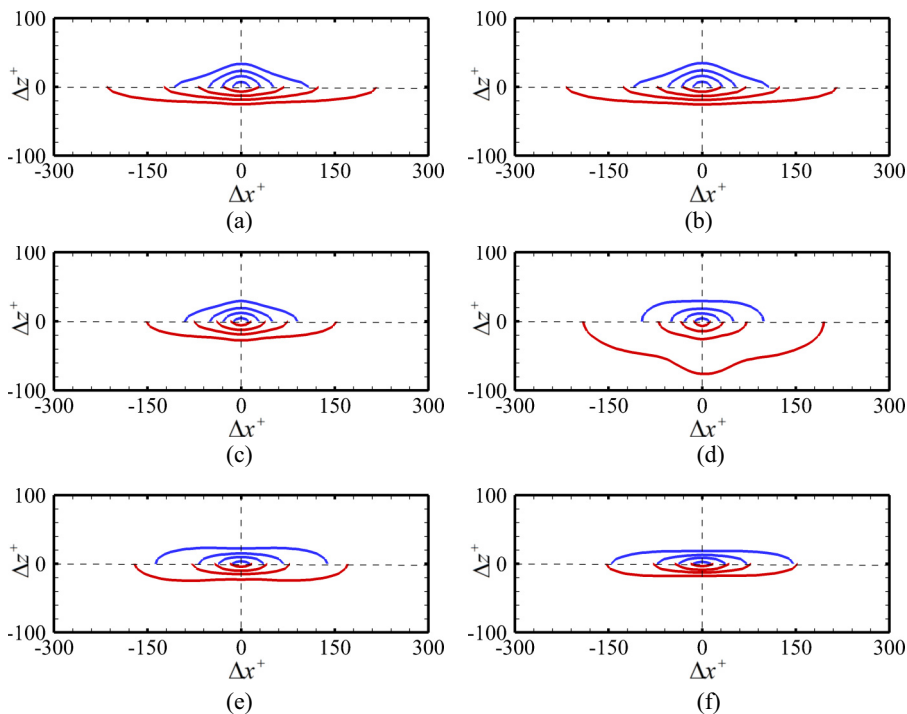


FIG. 14. Streamwise-spanwise correlation coefficients at various streamwise locations: (a)  $x_{\text{ref}}$ ; (b)–(f) S1–S5. Red:  $R_{\tau\tau}(\Delta x^+, \Delta z^+, 0)$ ; blue:  $R_{qq}(\Delta x^+, \Delta z^+, 0)$ . Four contour levels between 0.3 and 0.9 with an increment of 0.2 are shown.

where  $x_0$  is the reference streamwise location,  $\Delta x^+$  and  $\Delta z^+$  correspond to the spatial spacing in the streamwise and spanwise directions, respectively, and  $\Delta t^+$  is the time delay. Note that the axes in the correlation contours are on different scales, in order to better demonstrate the changes in the sizes of the energetic structures.

Figure 14 compares the contour lines of the streamwise-spanwise correlation coefficients  $R_{\tau\tau}(\Delta x^+, \Delta z^+, 0)$  and  $R_{qq}(\Delta x^+, \Delta z^+, 0)$  at six streamwise locations. At all of these locations, the isolines are clearly elongated in the streamwise direction for both  $\tau'$  and  $q'$ , with the streamwise extent of the contour map always being larger than its width, which supports that the streaky structures are well preserved through the curvature, as previously shown in Fig. 9. At  $x_{\text{ref}}$ , the comparison in Fig. 14(a) shows that the WSS field has a larger streamwise dimension and a smaller spanwise dimension than those of the WHF field. Taking the correlation level of 0.3 as an example, the spatial extents in the streamwise and spanwise directions are about  $\Delta x^+ = 440$  and  $\Delta z^+ = 52$  for  $\tau'$ , respectively, where  $\Delta x^+ = 210$  and  $\Delta z^+ = 68$  for  $q'$ . Importantly, the effect of curvature on the spatial dimension of  $R_{\tau\tau}(\Delta x^+, \Delta z^+, 0)$  is different from that of  $R_{qq}(\Delta x^+, \Delta z^+, 0)$ . In the  $x$  direction, we find that the spatial extent of the structures in  $\tau'$  generally decreases as the reference probe moves downstream, with the exception of an abrupt increase at location S3 [see Fig. 14(d)], whereas the sizes of the structures in  $q'$  appear to increase on the whole. In the  $z$  direction, the width of the correlations for the WSS field increases considerably in the concave region and decreases rapidly in the relaxation region, in contrast to the consistent decrease observed in the WHF field. As a consequence, the correlation map for  $\tau'$  at locations S5 has nearly the same spatial extent as that for  $q'$ , where  $\Delta x^+ = 296$  and  $\Delta z^+ = 36$ , as shown in Fig. 14(f). This finding provides evidence for the aforementioned strong similarities between the WSS and WHF fluctuations downstream from the curvature, as noted in Fig. 9.

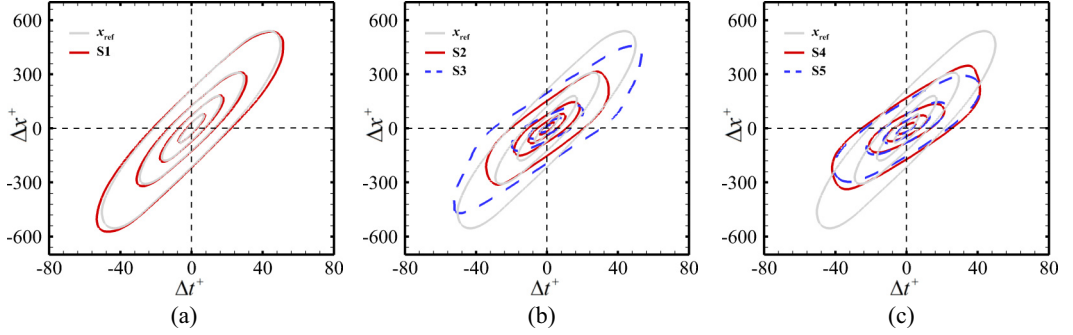


FIG. 15. Space-time correlation coefficients of the WSS fluctuations at various streamwise locations: (a) S1; (b) S2 and S3; (c) S4 and S5. Four contour levels are shown:  $R_{\tau\tau}(\Delta x^+, 0, \Delta t^+) = 0.2, 0.3, 0.5,$  and  $0.7$ . The gray isolines in (a)–(c) denote the results at  $x_{\text{ref}}$ .

The contour lines of the longitudinal space-time correlation coefficients  $R_{\tau\tau}(\Delta x^+, 0, \Delta t^+)$  and  $R_{qq}(\Delta x^+, 0, \Delta t^+)$  at the six locations are plotted in Fig. 15 for the WSS fluctuations and in Fig. 16 for the WHF fluctuations. The space-time organization of the WSS and WHF fields at  $x_{\text{ref}}$ , upstream of the curvature, is consistent with that observed in the zero-pressure-gradient compressible wall-bounded turbulence by Yu *et al.* [52]. It is characterized by a narrowed forward-leaning elliptical behavior, which is a clear indication of the strong downstream propagation of fluctuations. The correlations further confirm that the propagative nature of the fluctuations is independent of the presence of the curvature, with the skewed shape of the contours being well preserved at locations S1–S5. However, the main effect of the curvature is obviously a considerable reduction in the inclination angle for both  $\tau'$  and  $q'$ . In particular, the comparisons shown in Figs. 15(a) and 16(a) demonstrate that the space-time correlations at  $x_{\text{ref}}$  and S1 collapse well and that the inclination angles are slightly changed, except for small differences at larger separations, indicating a slow response of the fluctuations near the curvature onset. Throughout the curvature, it is evident that the inclined major axes become much closer to the axis of the delay time, and are more pronounced in the WHF field [see Fig. 16(b)], which reflects a dramatically decreased coherence along the rear part of the concave surface. After the curved region, it is clearly seen in Figs. 15(c) and 16(c) that the changes in the inclination angles at locations S4 and S5 are less significant but the angles are still lower than the upstream values, meaning that the recovery of the convection velocity is incomplete in the downstream relaxation region under the flow conditions investigated. It can be

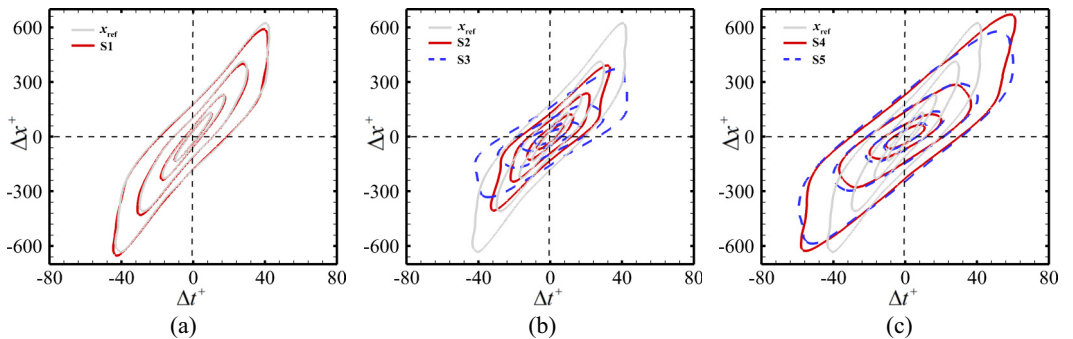


FIG. 16. Space-time correlation coefficients of the WHF fluctuations at various streamwise locations: (a) S1; (b) S2 and S3; (c) S4 and S5. Four contour levels are shown:  $R_{qq}(\Delta x^+, 0, \Delta t^+) = 0.2, 0.3, 0.5,$  and  $0.7$ . The gray contour lines in (a)–(c) denote the results at  $x_{\text{ref}}$ .

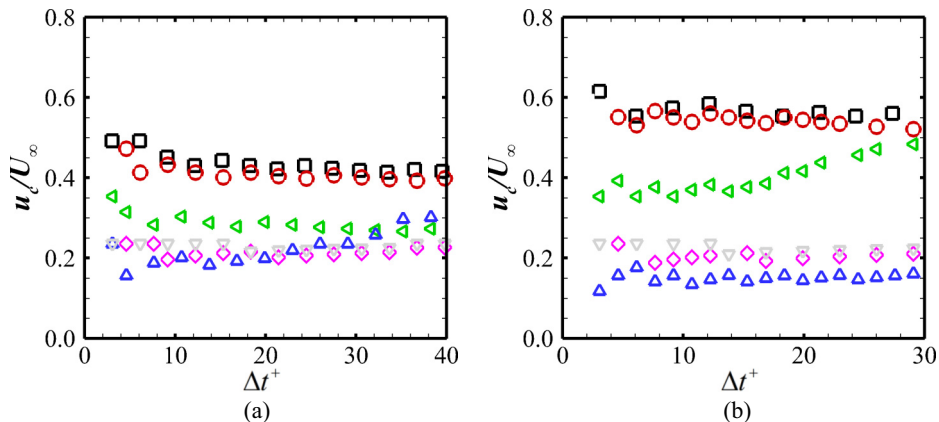


FIG. 17. The local convection velocity  $u_c$  as a function of the time delay  $\Delta t^+$  at various streamwise locations: (a) WSS; (b) WHF.  $x_{\text{ref}}$ : black squares; S1–S5: red circles, green left triangles, blue deltas, pink squares, and gray gradients.

reasonably inferred from this that the curvature has a large influence on the convection velocity of the fluctuating WSS and WHF.

To quantify the deceleration of the propagation caused by the curvature, the local convection velocities at the six streamwise locations, obtained from Figs. 15 and 16, are compared in Figs. 17(a) and 17(b) for  $\tau'$  and  $q'$ , respectively, as a function of the time delay  $\Delta t^+$ . Following Duan *et al.* [53] and Bernardini and Pirozzoli [54], the convection velocity  $u_c$  for a given time separation  $\Delta t^*$  is here computed as the ratio  $\Delta x^*/\Delta t^*$ , where the spatial separation  $\Delta x^*$  is taken at the point at which the space-time correlation  $R_{\tau\tau}(\Delta x, 0, \Delta t^*)$  or  $R_{qq}(\Delta x, 0, \Delta t^*)$  attains a local maximum. It is apparent at  $x_{\text{ref}}$  that the WHF fluctuations propagate downstream with speeds larger than those of the WSS fluctuations; that is,  $u_c = 0.55U_\infty$ – $0.62U_\infty$  for  $q'$  and  $u_c = 0.42U_\infty$ – $0.49U_\infty$  for  $\tau'$ . As expected, the convection velocities experience a remarkable decrease in the curved region, with the computed values at location S3 being about  $0.15U_\infty$ – $0.3U_\infty$  for  $\tau'$  and  $0.1U_\infty$ – $0.2U_\infty$  for  $q'$ . Interestingly, an asymptotic behavior is noticeable in the relaxation region, where the WSS and WHF fluctuations at locations S4 and S5 propagate at a similar speed of around  $u_c = 0.2U_\infty$ .

#### D. Frequency spectra

The wall frequency spectra at the six streamwise locations are plotted in Fig. 18 for the WSS and in Fig. 19 for the WHF as a function of the angular frequency  $\omega$ , to single out the effect of curvature on the energy distribution in frequency space. For comparison purposes, the frequency is normalized with respect to the reference viscous timescale  $\nu_w/u_\tau^2$ , with the kinematic viscosity at the wall  $\nu_w$  and the friction velocity  $u_\tau$  being taken at  $x_{\text{ref}}$ , whereas the spectra are normalized with respect to the local fluctuation intensity. The WSS and WHF fluctuations are sampled at a constant time interval of  $\Delta t u_\tau^2/\nu_w = 1.55$ , and thus the maximum Nyquist frequency is approximately  $\omega \nu_w/u_\tau^2 = 2.0$ . The power spectral density  $\psi(\omega)$  of the signal is estimated using Welch's algorithm with Hamming widows and a 50% overlap between successive segments. To further improve the statistical convergence of the estimated spectra,  $\psi(\omega)$  is averaged over 485 points in the  $z$  direction.

Regarding the WSS spectra, Fig. 18(a) shows that the premultiplied spectrum at  $x_{\text{ref}}$  is characterized by a single broadband peak centered at  $\omega \nu_w/u_\tau^2 = 0.07$ , which is coincident with previous findings for the WSS spectrum in low-speed TBLs at  $\text{Re}_\tau = 265 - 680$  by Daniel *et al.* [55] and channel flows up to  $\text{Re}_\tau = 1440$  by Hu *et al.* [56]. It is shown that the peak frequency is very insensitive to the curvature, but the peak magnitude varies significantly as the probe moves downstream, experiencing a large decrease in the curved region and a rapid increase in the relaxation

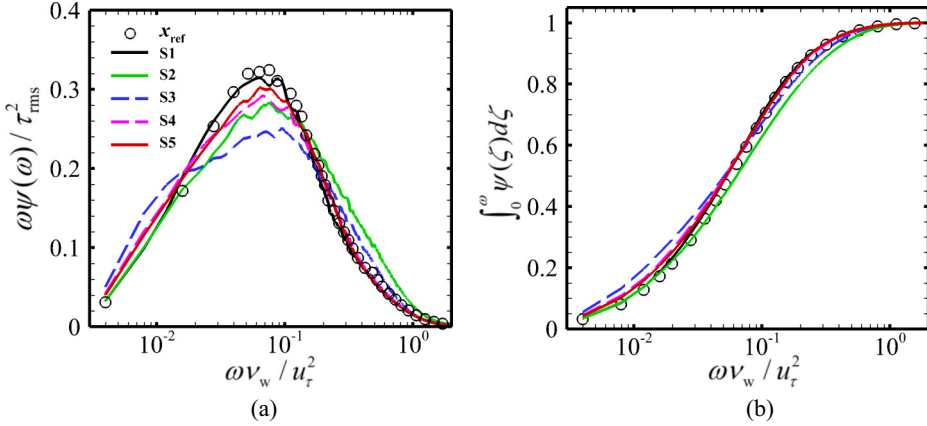


FIG. 18. Comparison of the WSS spectra at various streamwise locations: (a) the weighted power spectral density  $\omega\psi(\omega)$  on a log-linear plot; (b) the integration of power spectral density. The variable  $\tau_{\text{rms}}$  denotes the local WSS fluctuation intensity and the viscous timescale  $\nu_w/u_\tau^2$  is taken at  $x_{\text{ref}}$ .

region. Comparing the spectrum at location S5 with that at  $x_{\text{ref}}$ , it is apparent that the effect of curvature on the energy distribution among various frequencies becomes negligible. In contrast, the WHF spectra shown in Fig. 19(a) show significant curvature dependence. Upstream of the curvature, the dominant frequency occurs at  $\omega\nu_w/u_\tau^2 = 0.5$ , which is about seven times larger than that of the WSS spectra at  $x_{\text{ref}}$ . When the upstream turbulent boundary layer enters the concave surface, a shift toward lower frequencies is observed in the premultiplied WHF spectrum. It is seen that the energy at frequencies  $\omega\nu_w/u_\tau^2 \approx 0.2$  is remarkably enhanced and a distinct spectral peak located at  $\omega\nu_w/u_\tau^2 \approx 0.06$  emerges, which is very close to the central frequency of the peak in the WSS spectrum, whereas the energy at  $\omega\nu_w/u_\tau^2 \approx 0.3$  is attenuated. A more detailed view is given in Figs. 18(b) and 19(b), with the integrated spectra being compared below a specific frequency  $\omega$ . It is evident from Fig. 18(b) that all the curves collapse well, supporting a weak effect of curvature on the spectral energy in the WSS spectrum, whereas the curves at locations S3–S5 seen in Fig. 19(b) are obviously shifted to the left side of the figure, reflecting a strong amplification of the energy at

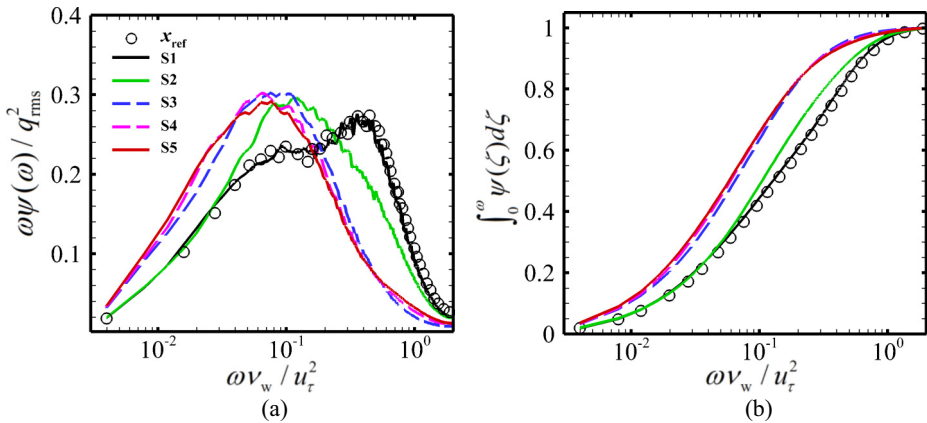


FIG. 19. Comparison of the WHF spectra at various streamwise locations: (a) the weighted power spectral density  $\omega\psi(\omega)$  on a log-linear plot; (b) the integration of the power spectral density. The variable  $q_{\text{rms}}$  denotes the local WHF fluctuation intensity and the viscous timescale  $\nu_w/u_\tau^2$  is taken at  $x_{\text{ref}}$ .

the lower frequencies. In particular, the portion of fluctuating energy in the range  $\omega \nu_w / u_\tau^2 \approx 0.2$  is gradually increased from about 60% at  $x_{\text{ref}}$  to 83% at locations S3–S5. Although the reason is not clear, the decrease in the dominant frequency  $\omega$  can be understood from the change in the convection velocity  $u_c$  and characteristic length scale  $\Lambda$ , assuming that  $\omega = 2\pi u_c / \Lambda$  still holds inside the concave boundary layer investigated here. The streamwise dimension in the spatial correlation analysis does not strictly reveal the typical size of the fluctuating WSS and WHF; however, it is a good indicator of the change in the characteristic length scale. Recalling the two-point space-time correlations seen in Figs. 14 and 17, since the presence of curvature leads to an increase in the streamwise extent and a decrease in the convection velocity, the observed spectral peak at lower frequencies is not surprising in the WHF field. On the other hand, the streamwise extent of the fluctuating WSS decreases throughout the curvature as well as the convection velocity, which reasonably explains the slight variation in the peak frequency.

### E. Decomposition of the mean WSS and WHF

In this section, the mean wall skin friction coefficients  $C_f$  at selected streamwise locations are decomposed to gain further insights into the mean WSS generation in the concave boundary layer. Following Li *et al.* [22], the decomposition formula for  $C_f$  in a compressible flow can be cast in the form

$$C_f = \overline{2\tau(x, z, t)} / \rho_\infty u_\infty^2 = C_{f,v} + C_{f,T} + C_{f,G}, \quad (5)$$

where

$$C_{f,v} = \frac{2}{\rho_\infty u_\infty^3} \int_0^\infty \bar{\tau}_{yx} \frac{\partial \tilde{u}}{\partial y} dy, \quad (6)$$

$$C_{f,T} = \frac{2}{\rho_\infty u_\infty^3} \int_0^\infty \bar{\rho} (-\tilde{u}'' \tilde{v}'') \frac{\partial \tilde{u}}{\partial y} dy, \quad (7)$$

$$C_{f,G} = \frac{2}{\rho_\infty u_\infty^3} \int_0^\infty (\tilde{u} - u_\infty) \left[ \bar{\rho} \left( \tilde{u} \frac{\partial \tilde{u}}{\partial x} + \tilde{v} \frac{\partial \tilde{u}}{\partial y} \right) + \frac{\partial}{\partial x} (\bar{\rho} \tilde{u}'' \tilde{u}'') - \bar{\tau}_{xx} \right] + \frac{\partial \bar{\rho}}{\partial x} dy. \quad (8)$$

The terms  $C_{f,v}$ ,  $C_{f,T}$ , and  $C_{f,G}$ , respectively, account for direct viscous dissipation, the power spent for turbulent kinetic energy production, and the streamwise heterogeneity. Note that  $\tau_{xx}$  in Eq. (8) and  $\tau_{yx}$  in Eq. (6) represent the streamwise components of the shear and the normal stress in the body intrinsic coordinate system, respectively.

Figure 20(a) shows the decompositions of  $C_f$  at selected streamwise locations. Throughout the curved ramp,  $C_f$  is decomposed with good accuracy, with the sum of the three terms on the right-hand side of Eq. (5) being very close to  $C_f$  (with the relative errors confined to  $\pm 1.0\%$ ). This confirms the high reliability of the forthcoming analysis. In agreement with the decomposed results of Fan *et al.* [24], the  $C_f$  generation at  $x_{\text{ref}}$  is typical of a canonical zero-pressure-gradient boundary layer, where positive  $C_{f,T}$  and positive  $C_{f,v}$  are predominant, contributing about 42% and 45% of  $C_f$ , respectively, and the small positive contribution of  $C_{f,G}$  is negligible. In the curved region ( $0 < X/\delta < 10$ ), the decomposition at location S1 is similar to that at  $x_{\text{ref}}$ , whereas differences are observed at locations S2 and S3, where the  $C_f$  generation is dominated by a balance of negative  $C_{f,G}$  and positive  $C_{f,T}$  (both with absolute values even larger than  $C_f$ ), and the positive  $C_{f,v}$  can be neglected. A similar trend was also reported by Fan *et al.* [57] in adverse-pressure-gradient TBLs. In the downstream relaxation region ( $X/\delta > 10$ ), the dominance of the positive  $C_{f,T}$  is preserved and the ratio  $C_{f,T}/C_f$  is decreased, but the decreased contribution of the negative  $C_{f,G}$  is gradually overtaken by that of the positive  $C_{f,v}$ . Moreover, the premultiplied integrands of  $C_{f,v}/C_f$ ,  $C_{f,T}/C_f$ , and  $C_{f,G}/C_f$  at different streamwise locations are shown as a function of  $y^+$  in Figs. 20(b)–20(d), respectively, to help further characterize the  $C_f$  generation. As shown in Fig. 20(b), most of the  $C_{f,v}$  contribution comes from the region  $y^+ < 30$ , regardless of the curvature. It is clear in Fig. 20(c) that the distributions of  $C_{f,T}/C_f$  are characterized by an inner peak around  $y^+ = 10$  and an outer

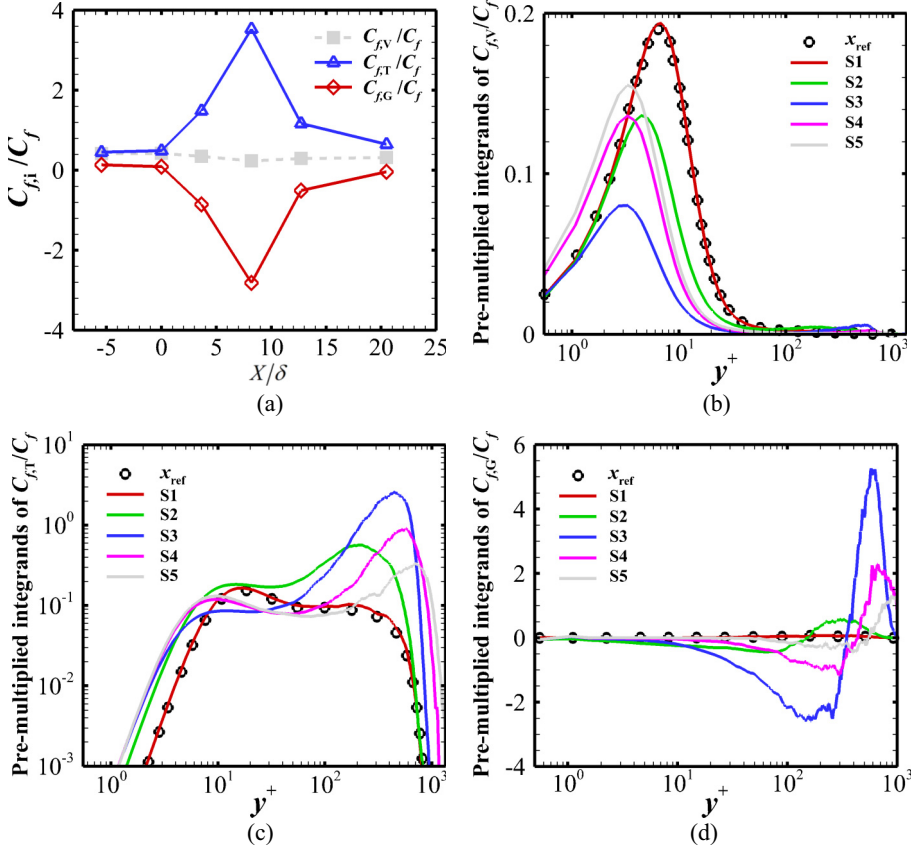


FIG. 20. (a) Contributions to  $C_f$  and (b)–(d) pre-multiplied integrands as a function of  $y^+$  at selected streamwise locations. (b)  $C_{f,v}/C_f$ ; (c)  $C_{f,t}/C_f$ ; (d)  $C_{f,g}/C_f$ .

peak at  $y^+ > 100$ , with the inner peak relatively insensitive to the curvature, whereas the magnitude of the outer peak significantly increases at locations S2–S5 and becomes much larger than that of the inner peak, implying that the fluctuations in the outer layer play an increasingly important role in the  $C_{f,t}$  contribution. This behavior will be discussed later in conjunction with a scale-based decomposition analysis based on the BEMD method. In addition, Fig. 20(d) shows that the counterbalance between the negative contribution from the inner region and the positive contribution within the outer layer is mainly responsible for the negative  $C_{f,g}$  contribution and the positive caused by the curvature, and the location of the sign switching is moved away from the wall as the probe is moved downstream.

Next, the decomposition formula for the mean wall heat transfer coefficient  $C_h$  proposed by Sun *et al.* [23] is used to investigate the effect of curvature on the mean WHF generation, which can be expressed as

$$C_h = \overline{q(x, z, t)}/\rho_\infty u_\infty^3 = C_{h,C} + C_{h,TH} + C_{h,MD} + C_{h,TKE} + C_{h,MS} + C_{h,RS} + C_{h,G}. \quad (9)$$

The seven terms on the right-hand side of Eq. (9) are explicitly expressed as follows:

$$C_{h,C} = \frac{1}{\rho_\infty u_\infty^4} \int_0^\infty k \frac{\partial \bar{T}}{\partial y} \frac{\partial \bar{u}}{\partial y} dy, \quad (10)$$

$$C_{h,TH} = \frac{1}{\rho_\infty u_\infty^4} \int_0^\infty -c_p \bar{\rho} \widetilde{v'' T''} \frac{\partial \bar{u}}{\partial y} dy, \quad (11)$$

$$C_{h,MD} = \frac{1}{\rho_\infty u_\infty^4} \int_0^\infty (\overline{u''\sigma_{xy}} + \overline{v''\sigma_{yy}}) \frac{\partial \tilde{u}}{\partial y} dy, \quad (12)$$

$$C_{h,TKE} = \frac{1}{\rho_\infty u_\infty^4} \int_0^\infty -\frac{1}{2} (\overline{\rho u'' u'' v''} + \overline{\rho v'' v'' v''}) \frac{\partial \tilde{u}}{\partial y} dy, \quad (13)$$

$$C_{h,MS} = \frac{1}{\rho_\infty u_\infty^4} \int_0^\infty (\tilde{u} \overline{\sigma_{xy}} + \tilde{v} \overline{\sigma_{yy}}) \frac{\partial \tilde{u}}{\partial y} dy, \quad (14)$$

$$C_{h,RS} = \frac{1}{\rho_\infty u_\infty^4} \int_0^\infty -\tilde{\rho} (\tilde{u} \overline{u'' v''} + \tilde{v} \overline{v'' v''}) \frac{\partial \tilde{u}}{\partial y} dy, \quad (15)$$

$$C_{h,G} = \frac{1}{\rho_\infty u_\infty^4} \int_0^\infty (\tilde{u} - u_\infty) \left[ \rho \frac{D\tilde{E}}{Dt} + \frac{\partial(\tilde{u}\tilde{\rho})}{\partial x} + \frac{\partial(\tilde{v}\tilde{\rho})}{\partial y} - \left( k \frac{\partial \tilde{T}}{\partial x} - c_p \tilde{\rho} \overline{u'' T''} + \overline{u'' \sigma_{xx}} + \overline{v'' \sigma_{yy}} \right. \right. \\ \left. \left. - \frac{1}{2} \overline{\rho u'' u'' u''} - \frac{1}{2} \overline{\rho v'' v'' u''} + \tilde{u} \overline{\sigma_{xy}} + \tilde{v} \overline{\sigma_{yy}} - \tilde{u} \overline{\rho u'' u''} - \tilde{v} \overline{\rho v'' u''} \right) dy \right]. \quad (16)$$

Here, the variables  $\sigma_{xx}$ ,  $\sigma_{xy}$ , and  $\sigma_{yy}$  denote the viscous stress components in the body intrinsic coordinate system. The terms  $C_{h,C}$ ,  $C_{h,TH}$ ,  $C_{h,MD}$ ,  $C_{h,TKE}$ ,  $C_{h,MS}$ , and  $C_{h,RS}$ , respectively, represent the contributions of the mean heat conduction, the turbulent heat transport, the wall-normal component of molecular diffusion, the turbulent kinetic energy transport, and the work of molecular stresses and Reynolds stresses. The term  $C_{h,G}$  accounts for the variation of the specific total energy  $\tilde{E}$  with time, the work of the pressure, and the streamwise heterogeneity.

Figure 21(a) shows the decompositions of  $C_h$  at selected streamwise locations. The sum of the seven terms on the right-hand side of Eq. (9) compares very well with  $C_h$  and the relative errors are confined to  $\pm 2.0\%$ , which serves as further confirmation of the accuracy of the present decompositions. As shown by Tong *et al.* [29], in the case of incident shock interactions under similar flow conditions, the  $C_h$  generation does not essentially change in character. At  $x_{ref}$ , it is clear that there are two dominant terms in the generation, a large positive  $C_{h,RS}$  and a large native negative  $C_{h,TH}$ , which contribute nearly 127% and  $-77\%$  of  $C_h$ , respectively, whereas the small contributions of the other terms are negligible, except for a relatively large contribution from  $C_{h,MS}$  (about 44% of  $C_h$ ). Throughout the curved ramp, we can see that the effect of curvature exhibits little influence on the balance between  $C_{h,RS}$  and  $C_{h,TH}$ , despite the two contributors experiencing a very large increase in magnitude, reaching about 276% and  $-177\%$  of  $C_h$  at location S3, respectively. It is reasonable to infer that the observed high  $C_h$  along the curved ramp surface [see Fig. 6(e)] is mainly caused by the combined action of the work of the Reynolds stresses and the turbulent transport of heat, with the excessive heat at the wall generated by the former being carried away from the wall toward the outer region through the latter, in a qualitatively similar way to that observed in a previous DNS of a spatially developing supersonic TBL by Tong *et al.* [25]. However, the most important difference can be obtained from the premultiplied integrands of the significant contributors shown in Figs. 21(b)–21(d), given that the proportions of  $C_{h,RS}$ ,  $C_{h,MS}$ , and  $C_{h,TH}$ , respectively, in the total mean WHF are accurately reflected by the areas beneath the respective curves. To be specific, the results in Figs. 21(b) and 21(d) reveal that beyond the curved region, the contributions coming from the near-wall region are no longer comparable to those related to the outer layer. The magnitude of the outer peak is significantly increased, in contrast to the decreased inner peak, and the peak gradually emerges at much higher wall-normal locations, leading to a dominant role of the outer layer in the contributions of  $C_{h,RS}$  and  $C_{h,TH}$ . The energization of the outer layer shown in Fig. 21(b) is consistent with what we found in the premultiplied integrand of  $C_{f,T}/C_f$  [see Fig. 20(c)], because of the high similarity between the integrands in Eqs. (7) and (15). Moreover, in Fig. 21(c), the energization of the outer layer is not observed, whereas the decreased contribution of  $C_{h,MS}$  is only associated with the inner layer around  $y^+ = 10$ .

To shed light on how turbulent structures contribute to the generation of  $C_f$  and  $C_h$ , we further break down the three dominant contributors,  $C_{f,T}$ ,  $C_{h,RS}$ , and  $C_{h,TH}$ , through a scale decomposition analysis, which is performed only along the  $z$  direction, as the flow in the  $x$ - $y$  plane is

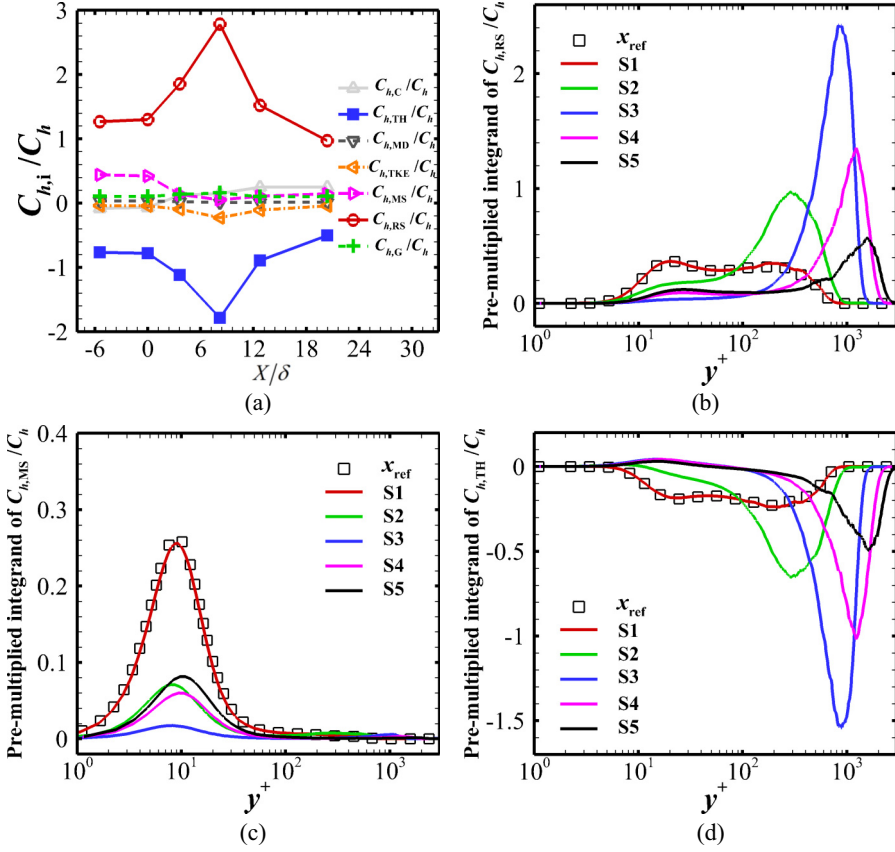


FIG. 21. (a) Contributions to  $C_h$  and (b)–(d) pre-multiplied integrands as a function of  $y^+$  at selected streamwise locations. (b)  $C_{h,RS}/C_h$ ; (c)  $C_{h,MS}/C_h$ ; (d)  $C_{h,TH}/C_h$ .

inhomogeneous. Similarly to Cheng *et al.* [58], we split the fluctuating velocity and temperature into their four BEMD modes

$$u'' = \sum_{i=1}^4 u_i'', \quad v'' = \sum_{i=1}^4 v_i'', \quad T'' = \sum_{i=1}^4 T_i'', \quad (17)$$

where  $u_i''$ ,  $v_i''$ , and  $T_i''$  are the decomposed fluctuations of the  $i$ th mode of the streamwise velocity, wall-normal velocity, and temperature, respectively. Under such a decomposition, the characteristic spanwise length scale for a given mode increases as the mode number increases. We now consider a simple decomposition of the Reynolds shear stress into 4 diagonal components and 12 nondiagonal components as

$$-\widetilde{u''v''} = -\sum_{i=1}^4 \widetilde{u_i''v_i''} - \sum_{i=1, j=1, i \neq j}^4 \widetilde{u_i''v_j''}, \quad (18)$$

where the first 4 diagonal components, denoted as (1, 1), (2, 2), (3, 3), and (4, 4), are related to fluctuations with specific spanwise length scales, whereas the last 12 nondiagonal components are produced by the interaction between the decomposed velocity fluctuations of the four modes, as identified by Cheng *et al.* [58] in turbulent channel flows. In particular, the first diagonal component (1,1) is associated with small-scale velocity fluctuations, and the fourth diagonal component (4,4)

is linked to large-scale velocity fluctuations, while the components (2,2) and (3,3) represent the contributions of intermediate-scale fluctuations. Substituting Eq. (18) into Eqs. (7) and (15), we have

$$C_{f,T} = \frac{1}{\rho_\infty u_\infty^3} \int_0^\infty -\bar{\rho} \widetilde{u_1'' v_1''} \frac{\partial \bar{u}}{\partial y} dy + \frac{1}{\rho_\infty u_\infty^3} \int_0^\infty -\bar{\rho} \widetilde{u_1'' v_2''} \frac{\partial \bar{u}}{\partial y} dy + \dots + \frac{1}{\rho_\infty u_\infty^3} \int_0^\infty -\bar{\rho} \widetilde{u_4'' v_3''} \frac{\partial \bar{u}}{\partial y} dy + \frac{1}{\rho_\infty u_\infty^3} \int_0^\infty -\bar{\rho} \widetilde{u_4'' v_4''} \frac{\partial \bar{u}}{\partial y} dy, \quad (19)$$

$$C_{h,RS} = \frac{1}{\rho_\infty u_\infty^4} \int_0^\infty -\bar{u} \bar{\rho} \widetilde{u_1'' v_1''} \frac{\partial \bar{u}}{\partial y} dy + \frac{1}{\rho_\infty u_\infty^4} \int_0^\infty -\bar{u} \bar{\rho} \widetilde{u_1'' v_2''} \frac{\partial \bar{u}}{\partial y} dy + \dots + \frac{1}{\rho_\infty u_\infty^4} \int_0^\infty -\bar{u} \bar{\rho} \widetilde{u_4'' v_3''} \frac{\partial \bar{u}}{\partial y} dy + \frac{1}{\rho_\infty u_\infty^4} \int_0^\infty -\bar{u} \bar{\rho} \widetilde{u_4'' v_4''} \frac{\partial \bar{u}}{\partial y} dy, \quad (20)$$

where the 16 terms on the right-hand sides of Eqs. (19) and (20) are their counterparts in Eq. (18). Note that the contribution of the wall-normal component of the Reynolds stresses in Eq. (15) is less than 5%, so it is neglected in Eq. (20). In a similar manner to that for the wall-normal heat flux, one can obtain the decomposition of  $C_{h,TH}$  as

$$C_{h,TH} = \frac{1}{\rho_\infty u_\infty^4} \int_0^\infty -c_p \bar{\rho} \widetilde{v_1'' T_1''} \frac{\partial \bar{u}}{\partial y} dy + \frac{1}{\rho_\infty u_\infty^4} \int_0^\infty -c_p \bar{\rho} \widetilde{v_1'' T_2''} \frac{\partial \bar{u}}{\partial y} dy + \dots + \frac{1}{\rho_\infty u_\infty^4} \int_0^\infty -c_p \bar{\rho} \widetilde{v_4'' T_3''} \frac{\partial \bar{u}}{\partial y} dy + \frac{1}{\rho_\infty u_\infty^4} \int_0^\infty -c_p \bar{\rho} \widetilde{v_4'' T_4''} \frac{\partial \bar{u}}{\partial y} dy. \quad (21)$$

In the following, we quantify the effect of curvature on the local contributions to  $C_{f,T}$ ,  $C_{h,RS}$ , and  $C_{h,TH}$  by comparing the decomposed results in the  $y$ - $z$  plane at three streamwise locations ( $x_{\text{ref}}$ , S2, and S5).

The premultiplied spanwise spectra of the streamwise velocity, wall-normal velocity, and temperature at various streamwise locations are shown in Fig. 22, and convincingly demonstrate the strong amplification of the outer large-scale fluctuations caused by the effect of curvature and the qualitative observation of the instantaneous vortical structures discussed in Fig. 8. Although the inner peak centered at  $y^+ \approx 13$  and  $\lambda_z^+ \approx 120$ , which is associated with the frequently quoted near-wall streaks, is slightly changed compared with that of  $x_{\text{ref}}$ , as shown in Figs. 22(a) and 22(d), the energy peak becomes apparent in the large ( $y^+$ ,  $\lambda_z^+$ ) domain. This corresponds to the large-scale energetic organization of the fluctuating streamwise velocity in the outer region of the distorted boundary layer, similar to that identified in the numerical study of Wu *et al.* [20]. Such an energization of the wall-normal velocity and temperature fluctuations in the outer region is clearly seen in Figs. 22(b) and 22(c), and 22(e) and 22(f), respectively, where the curvature has significantly increased the wall-normal location and width of the most energetic structures. It is shown that the primary inner peak, located in the small-wavelength region of the energy spectra at  $x_{\text{ref}}$ , loses its importance and vanishes completely at location S5, mainly due to the weakened near-wall turbulence activity, whereas a distinct energetic peak emerges in the outer large-wavelength region.

Figure 23 shows the energy spectra of the decomposed velocity and temperature fluctuations contained in each mode, with the full spectra calculated from the raw DNS data also included for comparison. It is clear that the full spectra are well covered by modes with consistently increasing spanwise length scales, implying the accuracy of the BEMD used. It can be concluded that the first mode is characterized by a strong peak located at  $\lambda_z^+ < 100$ , which corresponds to the small-scale fluctuations in the full flow field, whereas the energy peak of the fourth mode is at around  $\lambda_z^+ \approx 1000$  or  $\lambda_z \approx 1.3\delta$ , and is responsible for the energized large-scale motions. The typical spanwise length scales of the second and third modes are in the range  $100 < \lambda_z^+ < 1000$ , and can be assumed to represent intermediate-scale fluctuations. Another key observation is obtained from the variation of the wall-normal location of the spectral peaks. It can be seen in Figs. 23(a) and 23(b), and 23(d) and 23(e) that the peak location in the spectra of the decomposed velocity consistently

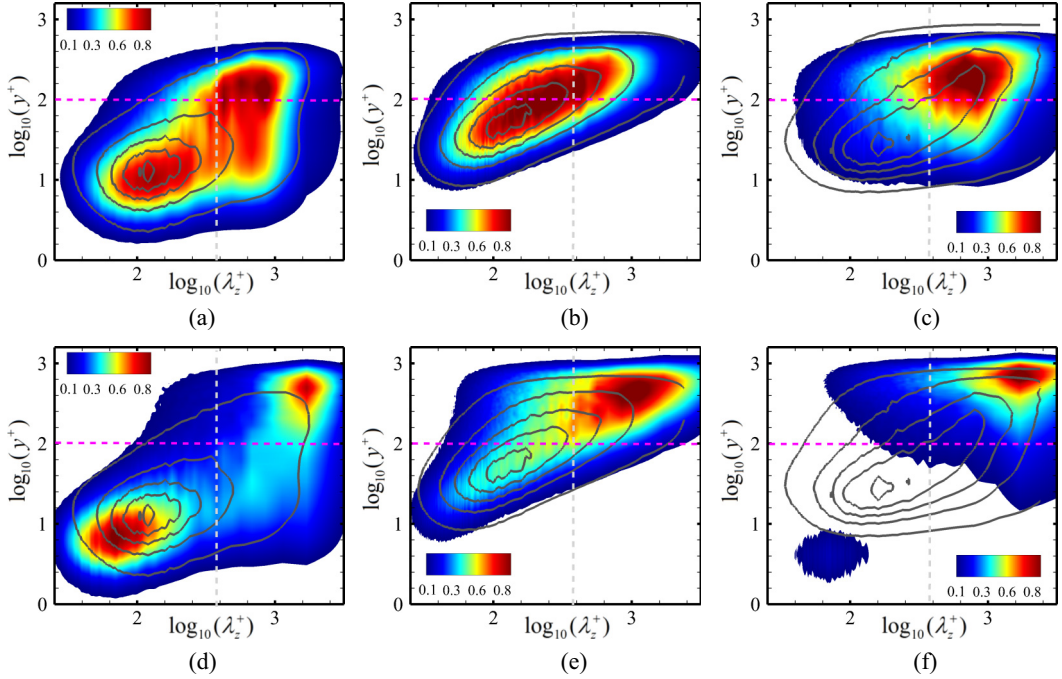


FIG. 22. Contours of the pre-multiplied spanwise spectra of fluctuations at locations S2 (upper panels) and S5 (lower panels): (a), (d) streamwise velocity; (b), (e) wall-normal velocity; (c), (f) temperature. The five isolines at levels 0.1, 0.3, 0.5, 0.7, and 0.9 are taken from  $x_{\text{ref}}$ . The spectra are normalized by the maximum value of each case. The horizontal and vertical dashed lines denote  $y^+ = 100$  and  $\lambda_z^+ = 479$  (or  $\lambda_z = 0.58$ ), respectively.

moves away from the inner region ( $y^+ \approx 6$ ) to the outer region ( $y^+ \approx 500$ ) as the mode number increases. However, the wall-normal locations of the spectral peaks, as seen in Figs. 23(c) and 23(f), are generally maintained at  $y^+ > 100$  and show a weak dependence on the mode number, except for the first mode in Fig. 23(f). This dissimilarity might be explained by a slower recovery of  $T''$  in the near-wall region, compared to those of  $u''$  and  $v''$ , since the full spectra of  $T''$  at locations S2 and S5 are mainly dominated by the large ( $y^+$ ,  $\lambda_z^+$ ) domain.

The decomposition of the Reynolds shear stress is shown in Fig. 24 as a function of  $y^+$  at locations S2 and S5. For both locations, the sum of the 16 components on the right-hand side of Eq. (18) collapses perfectly onto the wall-normal profile of the full Reynolds shear stress calculated using the raw DNS data, again confirming the high reliability of our decomposition. It is expected that the 4 diagonal components contribute most to the full profile, whereas the 12 nondiagonal components are negligible, which is consistent with the findings of previous studies by Tong *et al.* [26,29]. Among the four diagonal components, we note that the component (1,1) related to the small-scale fluctuations and the component (4,4) associated with the large-scale fluctuations are the two decisive factors in the Reynolds shear stress. At location S2, Fig. 24(a) shows that the component (1,1) attains its maximum value at  $y^+ \approx 17$  and is then overtaken by the component (4,4), which peaks at  $y^+ \approx 221$ . This supports the importance of the energized large-scale velocity fluctuations in the outer region for the generation of the Reynolds shear stress in the concavely curved flow presently studied. This finding is inconsistent with the decomposition at  $x_{\text{ref}}$  (not shown here), where the inner small-scale velocity fluctuations are dominant over the outer large-scale velocity fluctuations in the upstream TBL. From S2 to S5, the peak magnitude of the component (4,4) shown in Fig. 24(b) is amplified by a factor of about 2.5, with its peak positioned at  $y^+ \approx 523$ ,

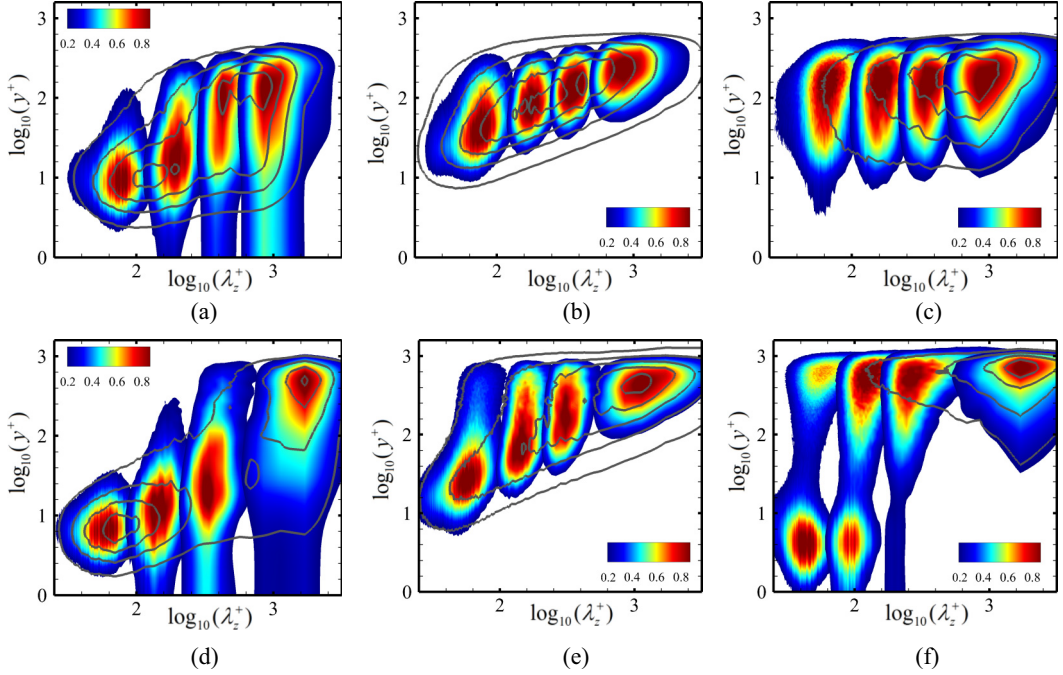


FIG. 23. Premultiplied spanwise spectra (colors) of the decomposed fluctuations in each mode together with the full spectra (black lines) at locations S2 (upper panels) and S5 (lower panels): (a), (d) streamwise velocity; (b), (e) wall-normal velocity; (c), (f) temperature. The spectra are normalized by the maximum values in each case. The black lines mark four isolines at levels 0.2, 0.4, 0.6, and 0.9.

while the component (1,1) increases slightly in the near-wall region and the other two diagonal components decrease significantly across the boundary layer. This behavior also suggests that downstream from the concave curvature, the outer large-scale velocity fluctuations are expected to have a much larger weight. With respect to the decomposition of the wall-normal heat flux at locations S2 and S5, the predominance of the diagonal components, and especially the absolute

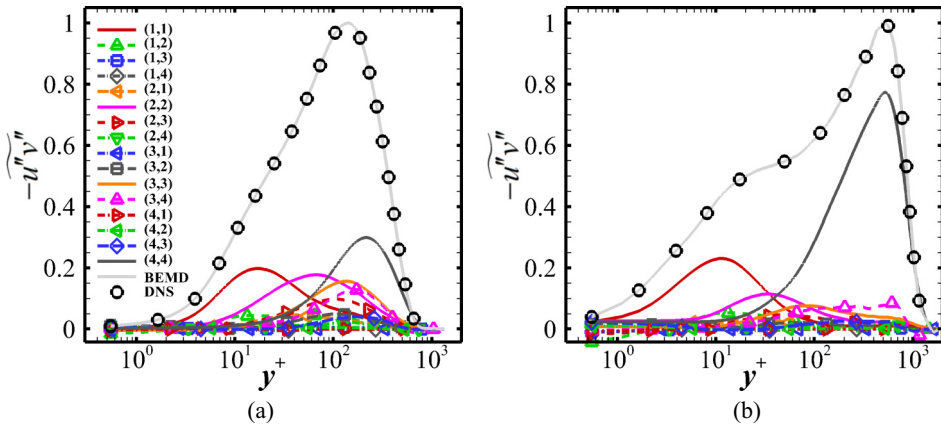


FIG. 24. Decomposition of the Reynolds shear stress at different streamwise locations: (a) S2; (b) S5. The profiles are normalized by the maximum value of the Reynolds shear stress.

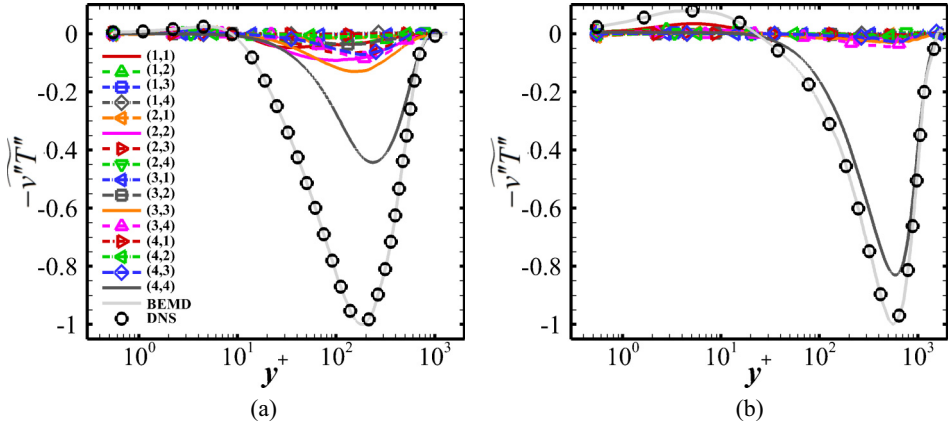


FIG. 25. Decomposition of the wall-normal heat flux at different streamwise locations: (a) S2; (b) S5. The profiles are normalized by the maximum value of the wall-normal heat flux.

importance of the component (4,4), is highlighted in Fig. 25. As shown in Fig. 25(a), the peak magnitude of the component (4,4) is roughly four times larger than those of the other three diagonal components, and it significantly increases at location S5, which is very close to the maximum value of the wall-normal heat flux at  $y^+ \approx 581$  [see Fig. 25(b)], implying a prominent role for the outer large-scale  $v''$  and  $T''$  fluctuations.

Figure 26(a) shows the contributions of the four diagonal components to  $C_{f,T}$ , as calculated using Eq. (19). At  $x_{\text{ref}}$ , the four diagonal components contribute about 72% of  $C_{f,T}$ , where the dominant component (1,1) provides up to 34%. This demonstrates that upstream of the curvature, the  $C_{f,T}$

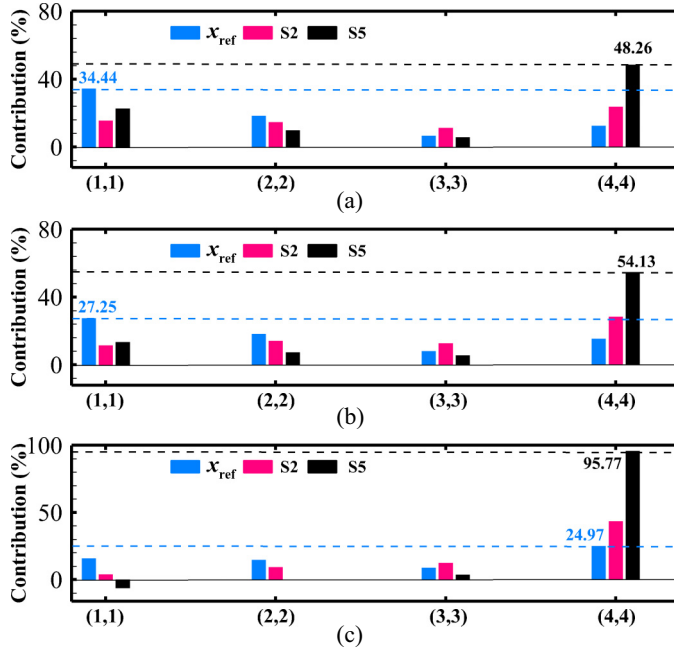


FIG. 26. Contributions of the four diagonal components at different streamwise locations: (a)  $C_{f,T}$ ; (b)  $C_{h,RS}$ ; (c)  $C_{h,TH}$ .

contribution is mainly generated by the near-wall small-scale  $u''$  and  $v''$  structures. At locations S2 and S5, despite most of  $C_{f,T}$  still coming from the four diagonal components, the significantly increased contribution of the component (4,4) reaches approximately 48% of  $C_{f,T}$ , which is much larger than the relatively decreased contribution of the component (1,1). For  $C_{h,RS}$ , Fig. 26(b) shows a similar trend, where the component (1,1) reaches up to 27% of  $C_{h,RS}$  at  $x_{ref}$ , whereas the component (4,4) accounts for nearly 54% of the work of the Reynolds stresses at location S5. Since  $C_{f,T}$  and  $C_{h,RS}$  are the leading positive contributions to  $C_f$  and  $C_h$ , respectively, it is believed that the generation of the mean WSS and WHF in the concave boundary layer is mostly associated with the energized outer large-scale velocity structures. Regarding the leading negative contribution to  $C_h$ , it can be seen from Fig. 26(c) that the  $C_{h,TH}$  generation is indisputably dominated by the component (4,4), whose contribution is consistently increased from 25% at  $x_{re}$  to 96% at S5, whereas the first three diagonal components always represent less than 15% (and even become negative at S5). This implies that throughout the curved ramp, the outer large-scale  $v''$  and  $T''$  structures are the sole determinant of the upward transport motion of the excessive heat at the wall.

#### IV. CONCLUSIONS

In the present study, we have performed DNS of a supersonic turbulent boundary layer at  $M_\infty = 2.25$  and  $Re_\tau = 769$  over a concavely curved compression ramp with a turning angle of  $24^\circ$  to investigate the effect of longitudinal concave surface curvature on the characteristics of WSS and WHF. Flow visualizations showed that the temperature field was increased significantly and a remarkable enhancement of the vortex structures was observed in the outer region of the distorted boundary layer. It was found that the mean WHF scaled well with the mean wall pressure in the concavely curved flow and the root-mean-square fluctuations in the WSS and WHF showed good collapse downstream from the curvature when scaled with the local mean values.

PDF analysis suggested that the strong correlation between the fluctuating WSS and WHF was less affected by the curvature, with the negative tail of the former becoming much wider and the opposite for the latter. A two-point correlation analysis showed that the effect of curvature had a clear impact on the streamwise coherence, leading to a decrease in the WSS field and an increase in the WHF field. The convection velocity of the downstream-propagating WSS and WHF fluctuations in the curved-wall flow was found to decrease significantly, reaching about  $0.2U_\infty$  in the downstream relaxation region. In addition, the premultiplied spectra showed that the characteristic frequency of the fluctuating WSS was very insensitive to the curvature, whereas the shape of the WHF frequency spectrum was qualitatively modified across the curved region, showing a shift to lower frequencies.

The mean WSS and WHF in the supersonic concavely curved ramp were decomposed using the identities proposed by Li *et al.* [22] and Sun *et al.* [23]. It was found that the effect of curvature essentially changed the generation mechanism of the mean WSS, with the dramatically increased contribution of  $C_{f,T}$  responsible for turbulence kinetic energy production balancing the contribution of  $C_{f,G}$  associated with the spatial growth of the flow, which became negative and large in the curved region. The generation mechanism of the mean WHF, which was dominated by the balance between the work of the Reynolds stresses  $C_{h,RS}$  and the turbulent transport of heat  $C_{h,TH}$ , remained practically unchanged, while the above two contributors were simultaneously increased. By performing a scale decomposition analysis of the velocity and temperature fluctuations based on the BEMD method, we quantitatively demonstrated that the curvature influenced the mean WSS and WHF generation largely by enhancing the contributions of outer large-scale structures.

#### ACKNOWLEDGMENTS

This work is supported by the National Natural Science Foundation of China (under Grant No. 11972356) and the National Key R&D Program of China (under Grant No. 2019YFA0405300). The authors would like to thank Yu Ming for his stimulating suggestions.

- [1] P. Bradshaw, Effects of streamline curvature on turbulent flow, Tech. Rep. AGARDograph 169 (1973).
- [2] A. J. Smits, The response of turbulent boundary layers to sudden perturbations, *Annu. Rev. Fluid Mech.* **17**, 321 (1985).
- [3] E. R. Spina, A. J. Smits, and S. K. Robinson, The physics of supersonic turbulent boundary layers, *Annu. Rev. Fluid Mech.* **26**, 287 (1994).
- [4] W. B. Sturek and J. E. Danberg, Supersonic turbulent boundary layer in adverse pressure gradient. Part I: The experiment, *AIAA J.* **10**, 475 (1972).
- [5] W. B. Sturek and J. E. Danberg, Supersonic turbulent boundary layer in adverse pressure gradient. Part II: Data analysis, *AIAA J.* **10**, 630 (1972).
- [6] A. J. Laderman, Adverse pressure gradient effects on supersonic boundary layer turbulence, *AIAA J.* **18**, 1186 (1980).
- [7] M. Jayaram, M. W. Taylor, and A. J. Smits, The response of a compressible turbulent boundary layer to short regions of concave surface curvature, *J. Fluid Mech.* **175**, 343 (1987).
- [8] P. H. Hoffmann, K. C. Muck, and P. Bradshaw, The effect of concave surface curvature on turbulent boundary layers, *J. Fluid Mech.* **161**, 371 (1985).
- [9] J. F. Donovan, E. F. Spina, and A. J. Smits, The structure of a supersonic turbulent boundary layer subjected to concave surface curvature, *J. Fluid Mech.* **259**, 1 (1994).
- [10] I. Neel, A. N. Leidy, R. D. W. Bowersox, and N. R. Tichenor, Hypersonic boundary layer with streamwise curvature-driven adverse pressure gradient, in *Eighth AIAA Flow Control Conference* (AIAA, Reston, VA, 2016), AIAA Paper No. 2016-4248.
- [11] Q. C. Wang and Z. G. Wang, Structural characteristics of the supersonic turbulent boundary layer subjected to concave curvature, *Appl. Phys. Lett.* **108**, 114102 (2016).
- [12] Q. C. Wang, Z. G. Wang, and Y. X. Zhao, An experimental investigation of the supersonic turbulent boundary layer subjected to concave curvature, *Phys. Fluids* **28**, 096104 (2016).
- [13] H. Thomann, Effect of streamwise wall curvature on heat transfer in a turbulent boundary layer, *J. Fluid Mech.* **33**, 283 (1968).
- [14] E. M. Fernando and A. J. Smits, A supersonic turbulent boundary layer in an adverse pressure gradient, *J. Fluid Mech.* **211**, 285 (1990).
- [15] D. R. Smith and A. J. Smits, A study of the effects of curvature and compression on the behavior of a supersonic turbulent boundary layer, *Exp. Fluids* **18**, 363 (1995).
- [16] Q. C. Wang, Z. G. Wang, and Y. X. Zhao, On the impact of adverse pressure gradient on the supersonic turbulent boundary layer, *Phys. Fluids* **28**, 116101 (2016).
- [17] F. L. Tong, X. L. Li, Y. H. Duan, and C. P. Yu, Direct numerical simulation of supersonic turbulent boundary layer subjected to a curved compression ramp, *Phys. Fluids* **29**, 125101 (2017).
- [18] M. B. Sun, N. D. Sandham, and Z. W. Hu, Turbulence structures and statistics of a supersonic turbulent boundary layer subjected to concave surface curvature, *J. Fluid Mech.* **865**, 60 (2019).
- [19] Q. C. Wang, Z. G. Wang, M. B. Sun, R. Yang, Y. X. Zhao, and Z. W. Hu, The amplification of large-scale motion in a supersonic concave turbulent boundary layer and its impact on the mean and statistical properties, *J. Fluid Mech.* **863**, 454 (2019).
- [20] X. S. Wu, J. H. Liang, and Y. X. Zhao, Direct numerical simulation of a supersonic turbulent boundary layer subjected to a concave surface, *Phys. Rev. Fluids* **4**, 044602 (2019).
- [21] G. L. Nicholson, J. J. Huang, L. Duan, and M. M. Choudhari, Simulation and modeling of hypersonic turbulent boundary layers subjected to adverse pressure gradients due to concave streamline curvature, in *AIAA Aviation Forum* (AIAA, Reston, VA, 2021), AIAA Paper No. 2021-2891.
- [22] W. P. Li, Y. T. Fan, D. Modesti, and C. Cheng, Decomposition of the mean skin-friction drag in compressible turbulent channel flows, *J. Fluid Mech.* **875**, 101 (2019).
- [23] D. Sun, Q. L. Guo, X. X. Yuan, H. Y. Zhang, and C. Li, A decomposition formula for the wall heat flux of a compressible boundary layer, *Adv. Aerodyn.* **3**, 33 (2021).
- [24] Y. T. Fan, W. P. Li, and S. Pirozzoli, Decomposition of the mean skin-friction drag in zero-pressure-gradient turbulent boundary layers, *Phys. Fluids* **31**, 086105 (2019).

- [25] F. L. Tong, S. W. Dong, J. Lai, X. X. Yuan, and X. L. Li, Wall shear stress and wall heat flux in a supersonic turbulent boundary layer, *Phys. Fluids* **34**, 015127 (2022).
- [26] F. L. Tong, S. W. Dong, J. Y. Duan, X. X. Yuan, and X. L. Li, Effect of expansion on the wall heat flux in a supersonic turbulent boundary layer, *Phys. Fluids* **34**, 105109 (2022).
- [27] F. L. Tong, X. X. Yuan, J. Lai, J. Y. Duan, D. Sun, and S. W. Dong, Wall heat flux in a supersonic shock wave/turbulent boundary layer interaction, *Phys. Fluids* **34**, 065104 (2022).
- [28] F. L. Tong, J. Y. Duan, and X. L. Li, Characteristics of reattached boundary layer in shock wave and turbulent boundary layer interaction, *Chin. J. Aeronaut.* **35**, 172 (2022).
- [29] F. L. Tong, J. Lai, J. Y. Duan, S. W. Dong, X. X. Yuan, and X. L. Li, Effect of interaction strength on recovery downstream of incident shock interactions, *Phys. Fluids* **34**, 1251274 (2022).
- [30] X. L. Li, D. X. Fu, and Y. W. Ma, Direct numerical simulation of hypersonic boundary layer transition over a blunt cone with a small angle of attack, *Phys. Fluids* **22**, 025105 (2010).
- [31] X. L. Li, D. X. Fu, and Y. W. Ma, Direct numerical simulation of hypersonic boundary-layer transition over a blunt cone, *AIAA J.* **46**, 2899 (2008).
- [32] F. L. Tong, D. Sun, and X. L. Li, Direct numerical simulation of impinging shock wave and turbulent boundary layer interaction over a wavy-wall, *Chin. J. Aeronaut.* **34**, 350 (2021).
- [33] X. K. Zhu, C. P. Yu, F. L. Tong, and X. L. Li, Numerical study on wall temperature effects on shock wave/turbulent boundary layer interaction, *AIAA J.* **55**, 131 (2017).
- [34] X. Chen, J. Q. Chen, and X. X. Yuan, Hypersonic boundary layer transition on a concave wall induced by low-frequency blowing and suction, *Phys. Fluids* **34**, 114105 (2022).
- [35] X. Chen, G. L. Huang, and C. Lee, Hypersonic boundary layer transition on a concave wall: Stationary Görtler vortices, *J. Fluid Mech.* **865**, 1 (2019).
- [36] M. P. Martin, E. M. Taylor, M. Wu, and V. G. Weirs, A bandwidth-optimized WENO scheme for the effective direct numerical simulation of compressible turbulence, *J. Comput. Phys.* **220**, 270 (2006).
- [37] S. Gottlieb and C. W. Shu, Total variation diminishing Runge-Kutta Schemes, *Math. Comput.* **67**, 73 (1998).
- [38] S. Pirozzoli and M. Bernardini, Turbulence in supersonic boundary layers at moderate Reynolds number, *J. Fluid Mech.* **688**, 120 (2011).
- [39] S. Priebe and M. P. Martin, Turbulence in a hypersonic compression ramp flow, *Phys. Rev. Fluids* **6**, 034601 (2021).
- [40] S. Pirozzoli, F. Grasso, and T. B. Gatski, Direct numerical simulation and analysis of a spatially evolving supersonic turbulent boundary layer at  $M = 2.25$ , *Phys. Fluids* **16**, 530 (2004).
- [41] E. J. Hopkins, E. R. Keener, T. E. Polek, and H. A. Dwyer, Hypersonic turbulent skin-friction and boundary-layer profiles on nonadiabatic flat plates, *AIAA J.* **10**, 40 (1972).
- [42] J. J. Huang, L. Duan, and M. M. Choudhari, Direct numerical simulation of hypersonic turbulent boundary layers: Effect of spatial evolution and Reynolds number, *J. Fluid Mech.* **937**, A3 (2022).
- [43] J. Fang, A. A. Zheltovodov, Y. F. Yao, C. Moulinec, and D. R. Emerson, On the turbulence amplification in shock-wave/turbulent boundary layer interaction, *J. Fluid Mech.* **897**, A32 (2020).
- [44] M. Eléna and J. Lacharme, Experimental study of a supersonic turbulent boundary layer using a laser Doppler anemometer, *J. Méc. Théor. Appl.* **7**, 175 (1988).
- [45] J. Jeong and F. Hussain, On the identification of a vortex, *J. Fluid Mech.* **285**, 69 (1995).
- [46] M. Grilli, S. Hickel, and N. A. Adams, Large-eddy simulation of a supersonic turbulent boundary layer over a compression-expansion ramp, *Int. J. Heat Fluid Flow* **42**, 79 (2013).
- [47] M. S. Loginov, N. A. Adams, and A. A. Zheltovodov, Large-eddy simulation of shock-wave/turbulent-boundary-layer interaction, *J. Fluid Mech.* **565**, 135 (2006).
- [48] R. L. Simpson, Turbulent boundary-layer separation, *Annu. Rev. Fluid Mech.* **21**, 205 (1989).
- [49] R. Örlü and P. Schlatter, On the fluctuating wall-shear stress in zero pressure-gradient turbulent boundary layer flows, *Phys. Fluids* **23**, 021704 (2011).

- [50] M. Yu, P. X. Liu, Y. L. Fu, Z. G. Tang, and X. X. Yuan, Wall shear stress, pressure, and heat flux fluctuations in compressible wall-bounded turbulence, Part I: One-point statistics, *Phys. Fluids* **34**, 065139 (2022).
- [51] H. Abe, H. Kawamura, and Y. Matsuo, Surface heat-flux fluctuations in a turbulent channel flow up to  $Re_\tau = 1020$  with  $Pr = 0.025$  and  $0.71$ , *Int. J. Heat Fluid Flow* **25**, 404 (2004).
- [52] M. Yu, P. X. Liu, Y. L. Fu, Z. G. Tang, and X. X. Yuan, Wall shear stress, pressure, and heat flux fluctuations in compressible wall-bounded turbulence, Part I: Spectra, correlation and nonlinear interactions, *Phys. Fluids* **34**, 065140 (2022).
- [53] L. Duan, M. M. Choudhari, and M. W. Wu, Numerical study of acoustic radiation due to a supersonic turbulent boundary layer, *J. Fluid Mech.* **746**, 165 (2014).
- [54] M. Bernardini and S. Pirozzoli, Wall pressure fluctuations beneath supersonic turbulent boundary layers, *Phys. Fluids* **23**, 085102 (2011).
- [55] C. D. Daniel, S. Laizet, and J. C. Vassilico, Wall shear stress fluctuations: Mixed scaling and their effects on velocity fluctuations in a turbulent boundary layer, *Phys. Fluids* **29**, 055102 (2017).
- [56] Z. W. Hu, C. L. Morfey, and N. D. Sandham, Wall pressure and shear stress spectra from direct numerical simulations of channel flow up to  $Re_\tau = 1440$ , *AIAA J.* **44**, 1541 (2006).
- [57] Y. T. Fan, W. P. Li, M. Atzori, R. Pozuelo, P. Schlatter, and R. Vinuesa, Decomposition of the mean skin-friction drag in adverse-pressure-gradient turbulent boundary layers, *Phys. Rev. Fluids* **5**, 114608 (2020).
- [58] C. Cheng, W. P. Li, A. Lozano-Durán, and H. Liu, Identity of attached eddies in turbulent channel flows with bidimensional empirical mode decomposition, *J. Fluid Mech.* **870**, 1037 (2019).